J. Fluid Mech. (1998), *vol.* 372, *pp.* 231–271. Printed in the United Kingdom

The coupling of waves and convection

By ANDREW P. STAMP[1]†, GRAHAM O. HUGHES[2]‡, ROGER I. NOKES[2]¶ AND ROSS W. GRIFFITHS[1]

[1]Research School of Earth Sciences, The Australian National University, Canberra, ACT 0200, Australia

[2]Department of Engineering Science, University of Auckland, Auckland, New Zealand

(Received 20 July 1996 and in revised form 5 May 1998)

Experiments with layers of salt and sugar solution separated by a diffusive interface are described. Interfacial waves were spontaneously generated by the convection once the system evolved to a critical value of the density-anomaly ratio $R_\rho \equiv \beta\Delta S/\alpha\Delta T$. The waves locally modulated the interfacial fluxes by modifying the interface thickness and thereby organized otherwise random convective motions into large-scale circulations. In turn, the waves themselves persisted for unusually long times owing to energy input from the organized convection. The dependence of the wave speed on the layer properties and channel dimensions was successfully predicted by assuming that coupling requires a matching of the wave and convection speeds, and that the system selects waves of an amplitude for which this resonance can occur. This 'wave–convection coupling' also appeared to increase the interfacial fluxes at low R_ρ. The interaction of waves and convection may be important for oceanic thermohaline staircases and other systems where convection is driven by interfacial fluxes.

1. Introduction

Waves are a common form of fluid motion, and can convey energy and momentum over large distances in gravitationally stable regions. Another well-known and important form of fluid motion is convection, which overturns fluid and transports heat from hot to cold regions. Occasionally, these two very different processes couple together and reinforce each other to produce dramatic phenomena. One such phenomenon is the 'El Niño–Southern Oscillation', which involves the coupling of waves in the equatorial ocean thermocline with atmospheric convective circulations in the southern hemisphere. A second example is atmospheric squall lines. These long-lived mesoscale flows result from interactions between a cold dense pool of air collapsing into a moist environment and convection driven by latent heating at the front of the cold pool. A somewhat different case is the coupling of large-amplitude waves and turbulent convection driven by fluxes through a double-diffusive interface. Here this flow is studied in the laboratory so as to provide a basis from which to develop a broader understanding of the processes by which waves and convection couple together.

† Present address: c/o McKinsey & Company, 24th Floor, 52 Martin Place, Sydney, NSW 2000, Australia.

‡ Present address: Research School of Earth Sciences, The Australian National University, Canberra, ACT 0200, Australia.

¶ Present address: School of Science and Computer Studies, Nelson Polytechnic, Private Bag 19, Nelson, NZ.

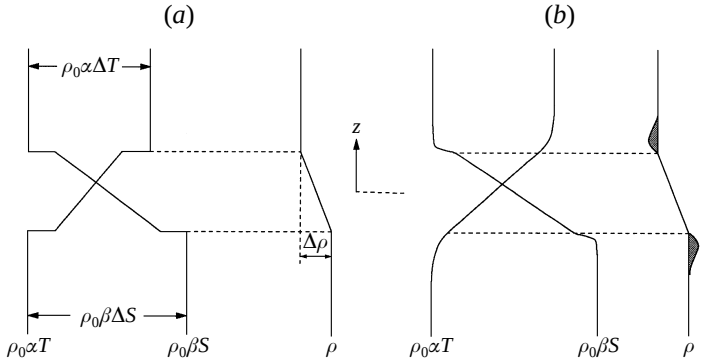

FIGURE 1. Structure of a diffusive interface. (*a*) A layer of fluid 'heavy in T' is poured on top of a denser layer 'heavy in S'. (*b*) Diffusion then acts to smooth the component gradients, and because $\kappa_T > \kappa_S$ the T interface thickens more rapidly than the S interface. With the stabilizing effect of the S stratification thus restricted, positively and negatively buoyant boundary layers form at the upper and lower edges of the interface.

Double-diffusive convection occurs when a fluid contains two or more components which diffuse at different rates and which make opposing contributions to the vertical density gradient. In such systems instabilities develop even when the initial density gradient is stable because diffusion, a stabilizing mechanism in single-component convection, acts to release the potential energy in the unstably stratified component. The exact form of the convection however, depends on whether the faster or slower diffusing component is unstably stratified. When the faster diffusing component is unstably stratified, an interface consisting of a stable 'diffusive' core between unstable boundary layers forms and drives two convecting layers (figure 1). Conversely, when the slower diffusing component is unstably stratified, the interface takes the form of an array of thin vertical counterflowing 'fingers'. Both types of convection are ubiquitous. The review articles of Turner (1974, 1985), Huppert & Turner (1981) and Schmitt (1994) report numerous oceanographic observations, as well as examples from such diverse fields as astrophysics, atmospheric physics, geology, liquid natural gas storage, solar pond heat reservoirs and materials science.

Turner (1965) performed the first experiments for the diffusive case, measuring the heat and salt fluxes across an interface formed by heating a stable two-layer salt-stratified fluid from below. He used dimensional reasoning to argue that the fluxes depend on the 4/3 power of the fractional density difference across the interface due to heat ($\alpha\Delta T$), together with a dependence on the density-anomaly ratio $R_\rho \equiv \beta\Delta S/\alpha\Delta T$, where $\beta\Delta S$ is the fractional density difference due to salt. In addition, Turner found that at low R_ρ interfacial transport was dominated by turbulent entrainment from the upper to the lower layer, whereas at high R_ρ molecular diffusion through the interfacial core accounted for the whole flux of each component. Numerous subsequent studies have focused on the fluxes through heat–salt interfaces (Linden 1974; Crapper 1975; Marmorino & Caldwell 1976; Taylor 1988; Kelley 1990). A diffusive interface can also form between two concentrated solutions at the same temperature, and Shirtcliffe (1973) demonstrated this using salt solution (now denoted by T, corresponding to the property that diffuses fastest) above sugar solution (S), for which the ratio of diffusivities is 1 : 3 compared to 1 : 100 for heat and salt. Linden & Shirtcliffe (1978) proposed a mechanistic model of double-diffusive transport across an interface that is in reasonable agreement with available experimental data.

This study considers the "systematic interfacial wavemotion coupled to large-scale convection in the layers" which occurs when a layer of salt solution lies above a layer of sugar solution (Turner & Chen 1974). Preliminary experiments showed that in this case the convection spontaneously generated large-amplitude 'waves' on the interface. These waves correspond to a local thickening of the interface and produced horizontal variations in the interfacial buoyancy flux, which in turn organized otherwise random convective motions by forcing circulations on the scale of the distance between waves. Subsequent interactions between the waves and convection led to a rapid decrease in the number of waves and an increase in the scale of the convective circulations. The waves themselves persisted for unusually long times owing to energy input from the organized convection. Similar 'wave–convection coupling' was also observed for cold fresh water above hot salt water and glycerol above an aqueous potassium carbonate solution, as well as for different tank and cell geometries.

To simplify the investigation, analysis was restricted to flows in rectangular channels with a single aqueous salt–sugar interface separating two layers of equal depth. A single wave formed once the system evolved to a critical value of the density-anomaly ratio, and propagated back-and-forth along the channel, organizing the convection in each layer into two cells which oscillated in length from zero to the full length of the channel. This cyclic flow continued for about 5 hours, during which time the average thickness of the interface increased, the buoyancy fluxes and convective velocities decreased, and in turn the wave speed decreased. The dependence of wave speed on the layer properties and channel dimensions was successfully predicted by assuming that effective coupling requires a matching of the wave and convection speeds, and that the system selects waves of an amplitude for which this resonance can occur.

This paper represents the combined effort of independent studies carried out by A.P.S. & R.W.G. at The Australian National University (ANU) and G.O.H. & R.I.N. at the University of Auckland (UA). A coherent presentation is made difficult by differences in experimental methods and results; however, a single paper seems the most judicious approach, with Stamp & Griffiths (1997) describing additional experiments carried out in an annulus. The structure of the paper is as follows. Section 2 describes the experiments. In § 3 a description of flows in rectangular channels with a single aqueous salt–sugar interface separating two layers of depth 11.5–12.0 cm is given. Section 4 gives the experimental plan and §§ 5 and 6 present measurements of the wave–convection coupling and interfacial fluxes for these flows. Section 7 briefly describes flows with different geometries and solutions.

2. Description of the experiments

The principal experiments carried out at ANU and UA both considered flows in rectangular channels driven by a single aqueous salt–sugar diffusive interface separating two layers of equal depth. This configuration was used because it was simple to set up and reduced the number of independent non-dimensional parameters. The two experimental programs did however use different channel geometries as well as different flow visualization and fluid sampling techniques. Although this makes a coherent presentation difficult, the different visualization techniques emphasized different aspects of the flow and thus proved advantageous.

2.1. *Experimental setup*

Previous studies have focused on the behaviour of diffusive interfaces formed by heating a stable two-layer salt-stratified fluid from below. In this configuration the

convective motions of the lower layer are dominated by the buoyancy flux through the bottom boundary rather than that through the diffusive interface. It is therefore not possible for interfacial waves to organize the convection. To overcome this limitation, diffusive interfaces have been formed by simply floating a layer 'heavy in T' on top of a denser layer 'heavy in S', so that the convection was entirely driven by the interfacial buoyancy flux. Salt water above sugar water was used. This choice allowed direct comparison with previous work and zero-flux boundary conditions to be achieved without the need for thermal insulation. Disadvantages were that viscosity was strongly dependent on sugar concentration, and that component concentrations could not be independently determined but had to be inferred from the measurement of two physical properties.

2.2. *Independent parameters*

Dimensional analysis indicates that the two-dimensional motions of a semi-infinite double-diffusive layer of Boussinesq fluid depend on: the T Rayleigh number

$$R_T = g\alpha\Delta T H^3/\nu\kappa_T, \tag{1}$$

the S Rayleigh number

$$R_S = g\beta\Delta S H^3/\nu\kappa_T, \tag{2}$$

the Prandtl number

$$Pr = \nu/\kappa_T \tag{3}$$

and the diffusivity ratio

$$\tau = \kappa_S/\kappa_T. \tag{4}$$

Here ΔT and ΔS are the salt and sugar concentration differences across the layer (defined > 0), $\alpha = \rho^{-1}(\partial\rho/\partial T)$ and $\beta = \rho^{-1}(\partial\rho/\partial S)$ are expansion coefficients which give the fractional density changes produced by unit changes in T and S, H is the layer depth, κ is the molecular diffusivity, ν is the kinematic viscosity, and g is the gravitational acceleration. For two layers with similar physical properties the only additional parameter is the depth ratio H_u/H_l, where hereinafter the subscripts u and l refer to the upper and lower layers. Finally, in laboratory experiments the influence of the tank geometry must also be taken into account, and tanks of rectangular horizontal cross-section $L \times w$ are characterized by the aspect ratios L/w and L/H_u. Hence, provided both layers have similar physical properties, the experimental setup can be defined within a seven-dimensional parameter space.

To simplify the investigation several parameters were eliminated. First, further constraints were imposed on the tank and layer geometries. All tanks were long and thin which allowed the dependence on L/w to be ignored; in reality this aspect ratio varied, $2.5 \leqslant L/w \leqslant 12$, but over this range the large-scale motions remained two-dimensional. Also, both layer depths were set to $11.5 \leqslant H \leqslant 12.0$ cm so that the depth ratio was unity. Second, only the aqueous salt–sugar system was used, and hence variations in physical properties were limited to those resulting from variations in the component concentrations. As a result it was assumed that both layers could be described by κ_T, κ_S and ν values for infinitely dilute solutions as well as α and β values at the mean concentrations $\overline{T}$ and $\overline{S}$, where hereinafter $\overline{(\,)}$ denotes a vertically averaged quantity. It follows that the Prandtl number and diffusivity ratio were constant.

In summary, this study examined the dependence of the flow on three non-dimensional parameters: the T Rayleigh number, S Rayleigh number and aspect

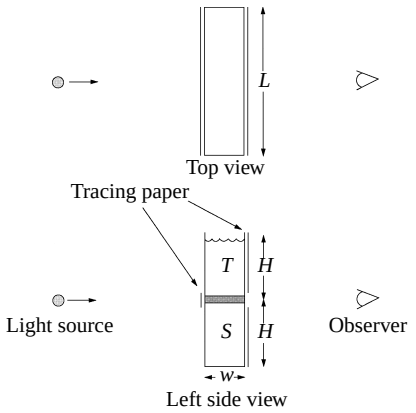

FIGURE 2. ANU experimental setup. Two large pieces of tracing paper were attached to the front of the tank so as to cover the upper and lower layers, and a thin strip of tracing paper was attached to the back of the tank to act as a diffusing screen behind the interface. This setup produced a shadowgraph of the convecting layers while allowing for direct observations of the interface.

ratio L/H. However, in practice the (non-dimensional) fractional density difference $\alpha\Delta T$ was used in place of R_T because under the described conditions all other constituent quantities were constant, and, as in other studies, the density-anomaly ratio $R_\rho \equiv \beta\Delta S/\alpha\Delta T$ was used in place of R_S.

2.3. *Apparatus and procedure – The Australian National University*

These experiments were carried out in glass channels with horizontal cross-sections ranging from $L \times w = 15 \times 5$ to 180×15 cm. Layer depths were chosen to be as large as possible, $H = 11.5$ cm, in order to produce the slowest rate of change of layer properties. This choice allowed observations to be made under quasi-steady conditions together with the most accurate determination of component concentrations.

Aqueous salt and sugar solutions were mixed to desired densities and left for a minimum of 12 hours to release any dissolved air and to equilibrate to room temperature (20 ± 2 °C). In some experiments small quantities of food dye or rheoscopic fluid (fish scales) were added to assist flow visualization. The lower (sugar) layer was then placed in the channel and the less dense upper (salt) layer floated on top through one or more diffusers. This procedure took between 5 and 60 minutes depending on the size of the tank. The diffusers were then removed, leaving a free upper surface, and the tank was sealed to prevent evaporation.

Throughout each experiment 2 ml samples were simultaneously withdrawn from the centre of both layers to allow the layer concentrations to be determined. The sampling interval was chosen to account for the decrease in fluxes with time, and typically ranged from 5 to 30 minutes. At most 2% of the total fluid was removed.

The standard setup used to visualize the flow is shown in figure 2. A 50 W slide projector illuminated the tank from the opposite side to that from which observations were made, i.e. the 'back' of the tank. Two large pieces of tracing paper were attached to the front of the tank so as to cover the upper and lower layers but not the interface. This setup produced a two-dimensional 'shadowgraph' of the two layers that revealed the convective motions, and emphasized the large-scale convective circulations and the plumes at the wave nose (figure 5). In addition, a thin strip of tracing paper was attached to the back of the tank to act as a diffusing screen behind the interface and thereby allow direct observations of the interfacial region to be made. The stable core

of the interface was distinguished as a green region between the yellow upper layer and blue lower layer, and it was possible to observe the time-dependent three-dimensional structure of the interface and sheet plumes. Finally, potassium permanganate crystals were occasionally dropped into the tank and distortion of the initially vertical dye lines noted. This technique was an excellent method of visualizing the large-scale convective circulations when there were several interfacial waves.

To supplement these observations, streak (long-exposure) photographs and time-lapse movies were taken. These techniques emphasized the long-time-scale motions associated with the large-scale convective circulations. Streak photographs were set up by adding a small amount of rheoscopic fluid to the layers and arranging projectors at both ends of the tank to illuminate a thin vertical cross-section of fluid. The resulting photographs showed the large-scale flow pattern of the convecting layers, and on occasions individual streaks were sufficiently distinct for accurate velocity estimates to be made.

2.4. *Apparatus and procedure – University of Auckland*

These experiments were carried out in acrylic tanks with horizontal cross-sections ranging from 25×5 to 150×10 cm, and filled with 12.0 cm deep layers in the manner described in § 2.3. To allow the layer concentrations to be determined, the density, conductivity and temperature of one layer were monitored throughout each experiment using probes connected to a computer. The density probe extracted fluid from the flow which was then passed through a digital densimeter before being returned to the flow. Two-dimensional schlieren images were used to visualize the flow, and, taking advantage of the refractive index variations within the fluid resulting from perturbations in the density field, revealed white boundary layers and plumes against a black background (figure 7).

2.5. *Estimation of salt and sugar concentrations*

The individual component concentrations of aqueous salt–sugar solutions cannot be measured, and must be inferred from measurements of two physical properties that respond differently to the two components. For this purpose, Ruddick & Shirtcliffe (1979) compiled a list of polynomials relating density, refractive index, conductivity and optical rotation to salt and sugar concentrations (in grams of solute per gram of solution) of aqueous solutions at 20 °C. At both ANU and UA density and conductivity were used. The density measurements gave an accurate estimate of the interfacial density difference, which was beneficial when comparing the observed waves with gravity current intrusions and internal solitary waves, as well as when estimating the interfacial buoyancy flux. Although conductivity tends to be less accurate than optical rotation and is affected by both components, it was more convenient and provided better concentration estimates than those inferred from density and refractive index measurements. Here a detailed description of the estimation procedure used at ANU is presented, with similar apparatus and procedures being used at UA.

Density was measured at 20.00 ± 0.01 °C using a digital densimeter (Anton Paar, K. G. Austria, Model DMA 02C) which gave a precision of $\pm 7 \times 10^{-5}$ g cm^{-3}. Conductivity was measured at room temperature using a four-wire conductivity probe (Precision Measurement Engineering, USA, Model MSCI-PME 106-300E), while simultaneous temperature measurements were made using a fast response glass thermistor (Fenwal Electronics, USA, Model 0.070 inch diameter). The measured conductivities were normalized to 20 °C assuming a 2.25% change per degree Celsius,

as is the case for salt solutions subject to small temperature deviations. This system gave a measured precision of $\pm 4\%$ over the range 5 to 150×10^{-3} mhos cm^{-1}.

In this manner, density and conductivity values at 20 °C were determined for each sample. Salt and sugar concentrations were then determined by inverting Ruddick & Shirtcliffe's (1979) polynomials using the suggested method. Errors in the polynomials and inversion process were small compared to the measurement errors. For lower layer solutions (i.e. low T, high S) measurement errors gave an uncertainty of ± 0.0004 g g^{-1} for T and ± 0.001 g g^{-1} for S, whereas for upper layer solutions (i.e. high T, low S) the uncertainties were an order of magnitude larger because of the percentage error in conductivity measurements. Furthermore, with conductivity strongly dependent on the salt concentration and weakly dependent on the sugar concentration, the change in conductivity between successive upper layer samples was less than that for the corresponding lower layer samples. Thus the influence of errors in concealing trends was also greater in the upper layer.

Fortunately, it was found that more accurate estimates of the salt and sugar concentrations in the upper layer could be inferred from the 'measured' lower layer concentrations using the conservation equations. In a two-layer system, conservation of mass, salt and sugar requires that

$$\rho_u H_u + \rho_l H_l = \text{constant}, \tag{5a}$$

$$\rho_u H_u T_u + \rho_l H_l T_l = \text{constant}, \tag{5b}$$

$$\rho_u H_u S_u + \rho_l H_l S_l = \text{constant}, \tag{5c}$$

and thus when ρ, T and S values are known for one layer the corresponding values for the other layer can be calculated. Furthermore, if the layer depths, densities and initial concentrations are well constrained, then properties estimated in this manner have similar uncertainties to the properties from which they are calculated. Here measurement errors produced poor estimates of T_u and S_u, and therefore T_l and S_l were used to calculate more accurate estimates of these properties. The layer depths were assumed constant, remaining unchanged to within ± 0.5 mm during experiments with no sampling and decreasing by less than 1.0 mm during experiments with sampling, and the initial concentrations were well constrained after being inferred from density measurements alone. In all experiments the T_u and S_u estimates calculated in this manner were consistent with those inferred from measurements.

In summary, accurate estimates of the salt and sugar concentrations in the lower layer were inferred from density and conductivity measurements, but this procedure produced poor estimates of the concentrations in the upper layer because of the percentage error in conductivity measurements. More accurate estimates of the upper layer concentrations were then inferred from the lower layer concentrations using the conservation equations. This technique resulted in similar uncertainties being appropriate for both layers. Formal error analysis suggests uncertainties of ± 0.0004 g g^{-1} for T, ± 0.001 g g^{-1} for S, ± 0.0004 for $\overline{\alpha}\Delta T$ and ± 0.01 for R_ρ, but the experimental data exhibits a precision an order of magnitude better.

3. Experimental observations

A number of preliminary experiments were carried out for familiarization with the experimental procedure and to determine the general nature of the flow. During each experiment the fixed quantities of salt and sugar were redistributed such that $\alpha\Delta T$ and $\beta\Delta S$ decreased, that is, salt moved from the upper to the lower layer and

sugar moved from the lower to the upper layer. With T being the more diffusive component $\alpha\Delta T$ decreased faster than $\beta\Delta S$, and therefore $R_\rho \equiv \beta\Delta S/\alpha\Delta T$ and $\Delta\rho/\rho_0 \equiv \beta\Delta S - \alpha\Delta T$ increased (figure 8). In response to this homogenization, the fluxes decreased, the convection weakened, the interface thickened and the flow evolved in a systematic manner. Over the first hour the convection became progressively more two-dimensional and organized the interface into thick and thin regions. Following this, a single thick region of interface formed and propagated back-and-forth along the channel, modulating the fluxes and organizing the convection into large-scale circulations. Here observations of the experiments are presented, with measurements given for those started at low R_ρ in the 15×5 cm channel.

3.1. *Filling disturbances*

Despite the care taken when floating the upper layer on top of the lower layer, this procedure always generated disturbances. Three types of filling disturbances occurred. First, mixing at the interface produced intermediate density fluid, which was then entrained into the layers at a rate dependent on the strength of the convection. Second, when multiple diffusers were used, it was difficult to maintain equal inflow rates, and horizontal differences in density and composition were set up in both layers. These gradients led to large-scale convective circulations but were soon destroyed by the convection. Finally, while removing diffusers, the interface was occasionally displaced and thereby set into a slow seiching motion. Such oscillations were rapidly damped by friction.

Mixing occurred in all experiments; when using diffusers with low inflow rates the upper layer density decreased below that of the inflow causing overturning, whereas with high inflow rates mixing occurred because of the downward momentum of the inflow. The amount of mixing and the subsequent behaviour of the flow depended on the conditions. At low R_ρ, the convection was sufficiently vigorous to entrain all of the mixed fluid, and thus the interface remained thin (< 1 mm) and there was no start-up period in the fluxes. In contrast, at high R_ρ the convection could only entrain some of the mixed fluid and a uniformly thick (10 mm) stably stratified interface formed. A period of inactivity followed, during which diffusion re-established the double boundary layer structure of the interface, and then convection slowly restarted (figures 8*c* and 15). Thereafter the convection eroded the interface and the fluxes increased, so that within an hour the flow was indistinguishable from that of experiments started with little mixing.

In summary, the flow behaved in the same manner for experiments carried out with different filling techniques and different tank geometries, indicating that the long-term behaviour did not depend on the conditions imposed during filling. For example, experiments ANU1.6*a, b* exhibited identical behaviour after both were started with the same solutions using different filling techniques.

3.2. *Transient behaviour*

After the mixed fluid was entrained and vigorous convection established, the fluxes began to decrease, and in turn the convection became weaker allowing the interface to thicken by diffusion. For experiments started at low R_ρ this evolution began with a period of transient behaviour characterized by three distinct flow regimes.

The first transient flow regime is shown in figure 3(*a, b*). This regime occurred when $R_\rho < 1.10$, and was governed by a balance between the production of stable interfacial core fluid and its entrainment into the layers by the convection. The flow

was characterized by a uniformly thin interface (< 1 mm), small three-dimensional convection cells and vigorous three-dimensional convective motions.

After about 30 minutes the convection became too weak to entrain all the interfacial fluid produced, and within 5 minutes the interface thickened and the flow changed to that shown in figure 3(*c,d*). The interface remained thin everywhere except at the base of the plumes, where it was about 2 mm thick, and the plumes became aligned across the channel forming small two-dimensional cells but continuing to drive three-dimensional motions. This second transient flow regime occurred when $1.10 \leqslant R_\rho < 1.13$ and, as such, lasted for about 15 minutes. During this time a large amount of interfacial fluid was produced and all this fluid was swept to the base of the plumes, and the convection thereby organized the interface into thick and thin regions.

The third transient flow regime is shown in figure 3(*e,f*) and occurred when $1.13 \leqslant R_\rho < 1.15$. The flow was characterized by large thick regions of interface at the base of the plumes, large two-dimensional cells and two-dimensional motions. In general, these interfacial 'lumps' extended across the channel and were about 4 mm thick and 2–5 cm long, while elsewhere the interface remained < 1 mm thick. The variations in the thickness of the interface produced variations in the interfacial gradients of T and S, and hence variations in the interfacial fluxes. Thus the thick (small gradient) regions produced less marginally unstable boundary layer fluid and stable interfacial core fluid than the thin (large gradient) regions. Nevertheless, the flow was stable because the stress exerted by the convection stopped the lumps spreading out under the restoring force of gravity.

Initially the number of interfacial lumps depended on the channel length, increasing from 2 to 10 as the length increased from 15 to 180 cm. However, as the lumps moved back-and-forth collisions occurred, and with large lumps engulfing small lumps during head-on collisions and lumps merging during overtaking collisions, the number of lumps decreased with time. When the final two lumps collided near an endwall, the high fluxes along the thin interface extending to the opposite endwall set up horizontal density gradients within the layers that led to tank-scale convective circulations. The two lumps then merged and propagated back along the channel. This merging occurred about 15 minutes after the start of the third transient flow regime and signified the end of the transient behaviour.

3.3. *Long-term cyclic behaviour*

Once a single large thick region of interface formed, the nature of the flow changed to that shown in figures 4 to 7. This wave propagated back-and-forth along the channel modulating the fluxes and organizing the convection into large-scale circulations, which reversed direction quasi-periodically. With the exception of flows in very long channels, changes in layer properties during each cycle were negligible. The behaviour of one such quasi-steady cycle will now be described.

A convenient point at which to begin the description is shown in the top frame of each figure. The thick region of interface propagated to the right, while intense plumes at the nose (leading edge) drove two large-scale counter-rotating convection cells in each layer. Marginally unstable boundary layer fluid was produced throughout the thin interface ahead of the wave; however advection by the cells concentrated plumes at the nose. Meanwhile, diffusion re-established the double boundary layer structure of the thin interface left in the wave's wake. The wave propagation was assisted by the cells along its length but hindered by the cells ahead.

The convection evolved in response to the propagation of the wave. As the nose

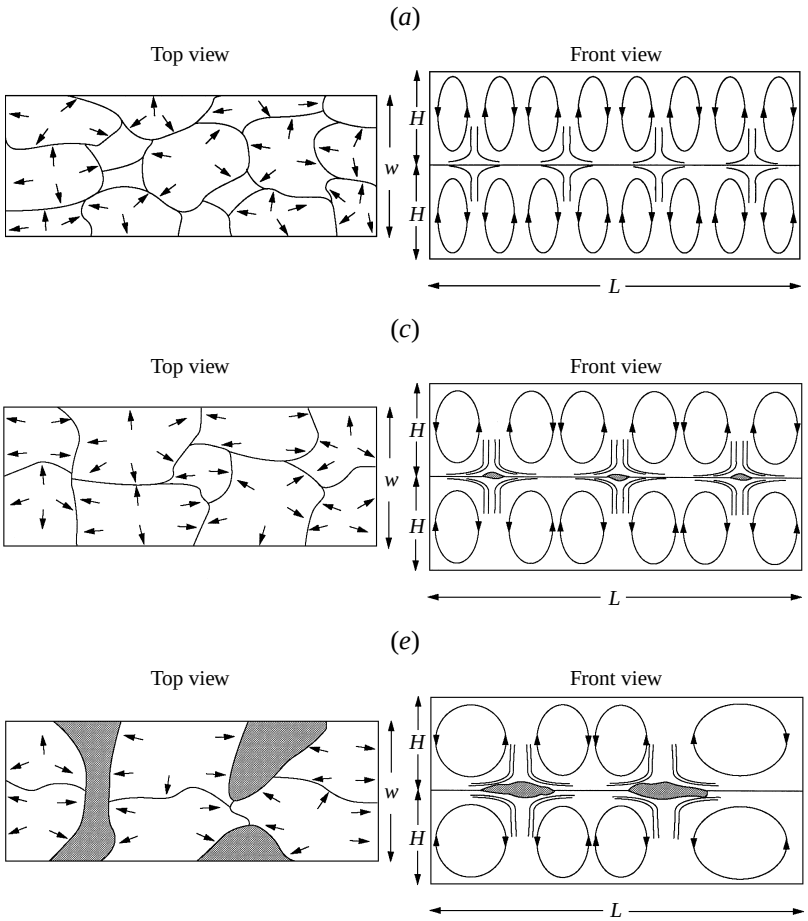

FIGURE 3(*a*, *c*, *e*). For caption see facing page

approached the endwall, the size and strength of the cells along the wave increased at the expense of the cells ahead of the wave. In turn, this change in the convection tended to accelerate the wave, particularly away from the sidewalls where the convection was strongest. Thus the leading and trailing edges of the wave formed a ∪ shape across the channel width, instead of the purely two-dimensional structures associated with gravity current intrusions and internal solitary waves in the absence of ambient motions.

In general, the wave extended along half the channel as a long thin tail attached to a short thick nose (figures 5 to 7). The tail was about 2 mm thick and looked like a continuous stream of well-mixed fluid, whereas the nose was about 4 mm thick and 10 mm long and looked like a lump of well-mixed fluid. However, the profile and speed of the wave fluctuated in response to changes in the convection, and occasionally the nose appeared as a wedge-like extension of the tail.

When the wave collided with the endwall the plumes at the nose were cut off and the cells ahead of the wave disappeared, leaving a single tank-scale cell in each layer. These cells continued to sweep both the wave and any plumes developing along the interface against the endwall. This sweeping created a symmetric wedge of interfacial fluid which continued to pile up against the endwall until it extended over

(*b*)

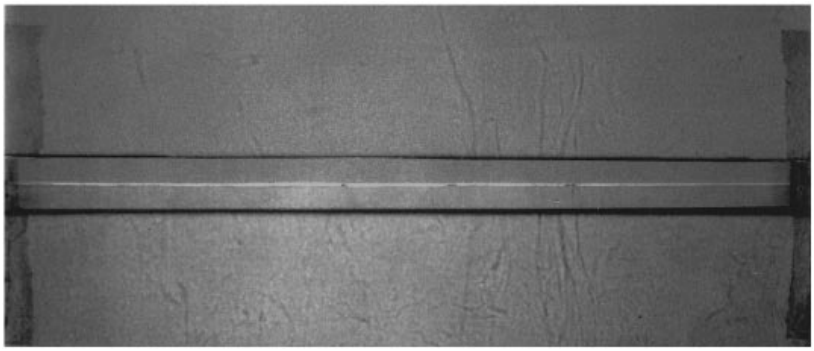

(*d*)

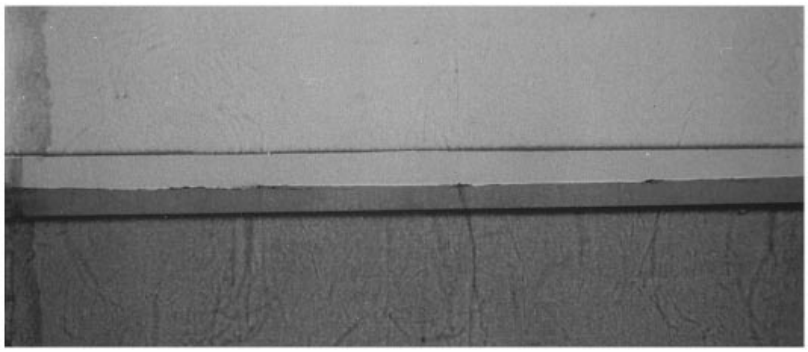

(*f*)

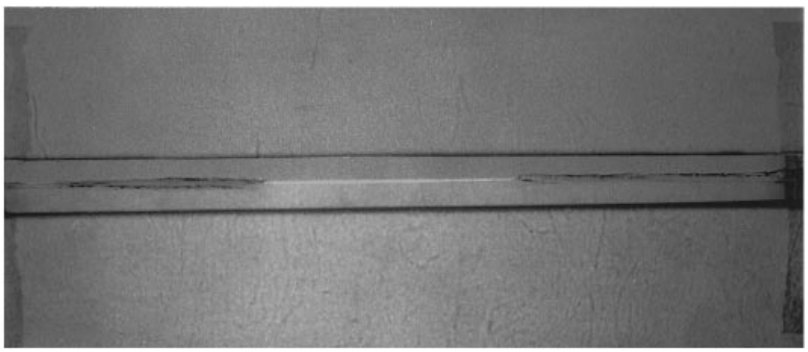

FIGURE 3. Transient behaviour: illustrations and photographs of the (*a, b*) first, (*c, d*) second and (*e, f*) third transient flow regimes. Initially the interface was thin and large fluxes drove vigorous three-dimensional convection; however, as the layer properties changed, the fluxes decreased, the convection became weaker and more two-dimensional while the interface became organized into thick and thin regions.

less than half the channel length. Meanwhile, a bulge corresponding to the reflected nose propagated back through the tail.

Eventually a distinct lump of well-mixed fluid appeared at the left end of the thick interfacial region and propagated slowly to the left. The origin of this feature varied; in short channels its appearance coincided with the emergence of the reflected

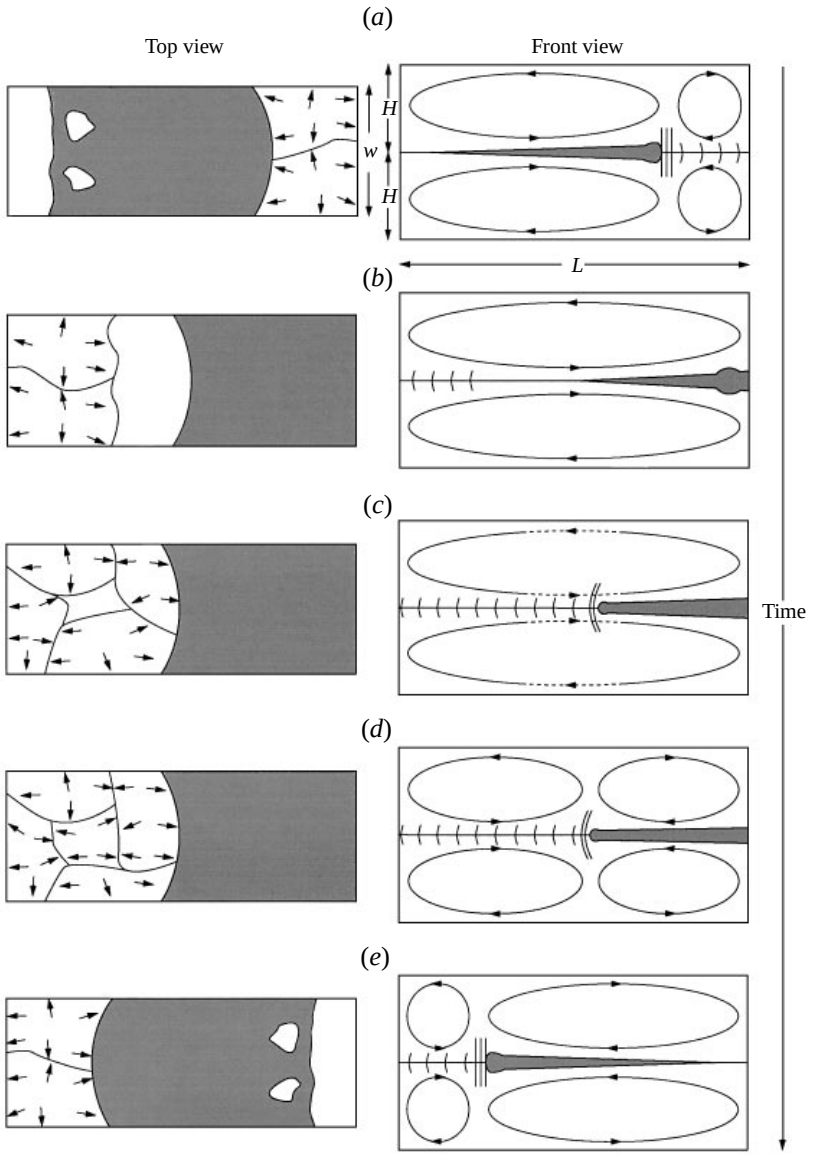

FIGURE 4. A quasi-steady cycle is shown. (*a*) The wave propagates to the right while intense plumes at the nose drive two large-scale counter-rotating convection cells in each layer. (*b*) When the wave collides with the endwall, the plumes at the nose are cut off leaving a single tank-scale cell in each layer. These cells sweep the interfacial fluid against the endwall, but a bulge corresponding to the reflected nose propagates back through the tail. (*c*) Eventually, the nose appears at the left end of the wave and as it progresses the interfacial fluid trapped against the endwall collapses under gravity and the plume activity at the nose increases. (*d*) On reaching the centre of the channel, the plumes at the nose have destroyed the tank-scale cells and re-established two counter-rotating cells in each layer. (*e*) Moments later the tail detaches from the endwall. The cycle then repeats.

nose, whereas in long channels it appeared to be a new feature. Nevertheless, in both cases the nose propagated along the interface, making greatest progress at the sidewalls where the opposing convection was weakest. At the same time the interfacial fluid trapped against the endwall collapsed under gravity. The nose became

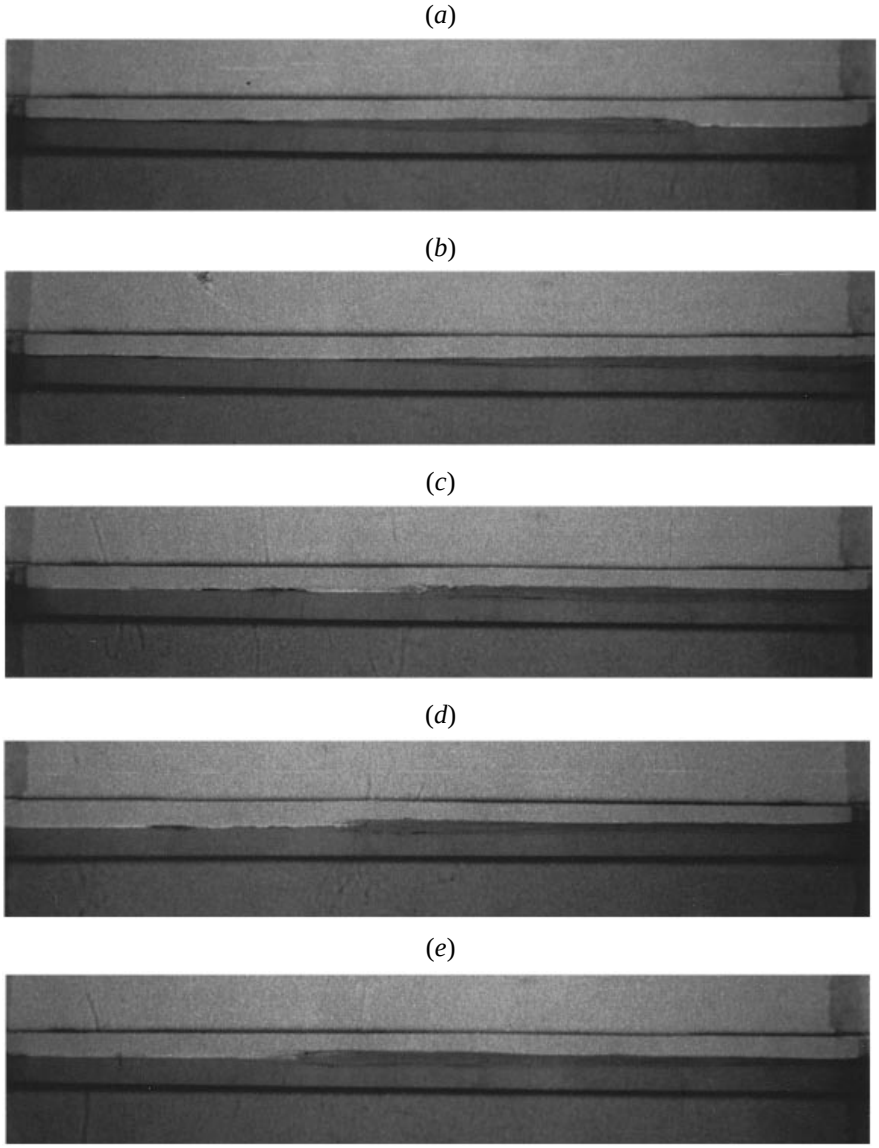

FIGURE 5. Direct photographs of a quasi-steady cycle: (*a–e*) correspond to figure 4.

more lump-like, and in response the plume activity at the nose increased, which weakened the large-scale circulation behind the nose. This change in the convection allowed more of the trapped interfacial fluid to escape and accelerate away from the endwall.

By the time the nose reached the centre of the channel the plumes at the nose had destroyed the tank-scale cells, and re-established two large-scale counter-rotating cells in each layer. This flow swept fluid away from the endwall and when the nose was just past the centre of the channel the tail detached from the endwall. The cycle then repeated.

(*a*)

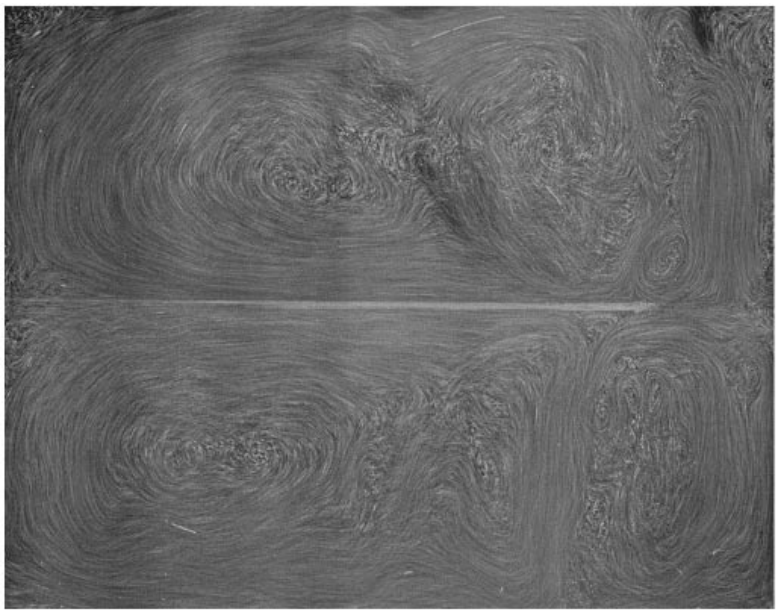

(*b*)

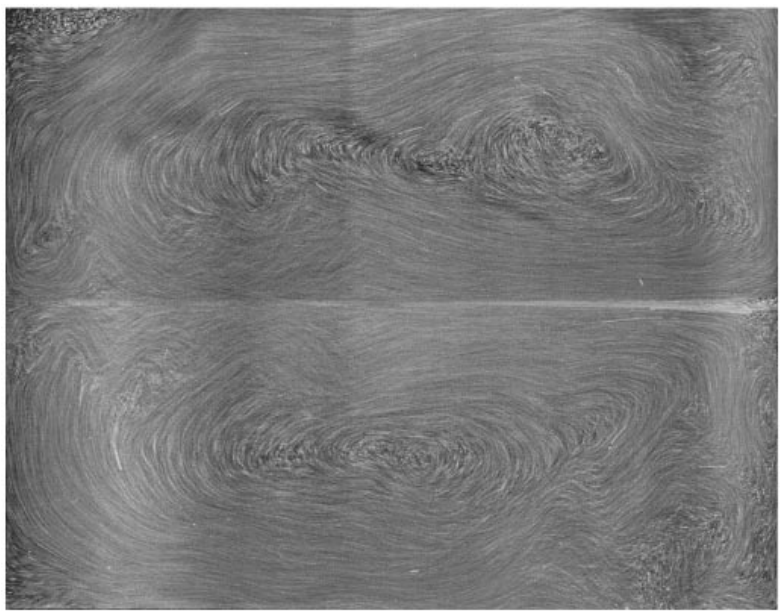

FIGURE 6(*a*, *b*). For caption see facing page.

3.4. *Run-down behaviour*

This cyclic flow continued for about 4 hours, during which time there was a two-fold decrease in $\alpha\Delta T$ and R_ρ increased from 1.15 to 1.40 (table 1). However, whilst the qualitative behaviour of the flow remained unchanged, several quantitative aspects changed: the thickness of the thin region of interface increased, the length of the thick

(*c*)

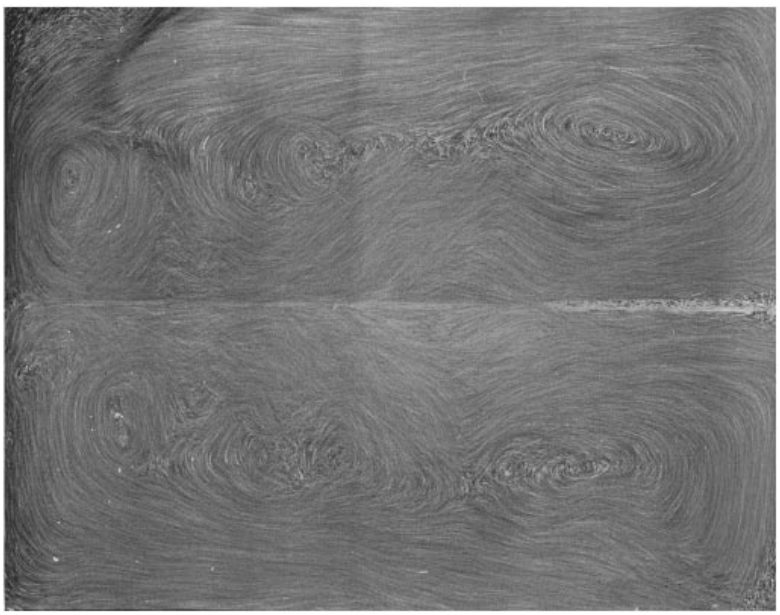

(*d*)

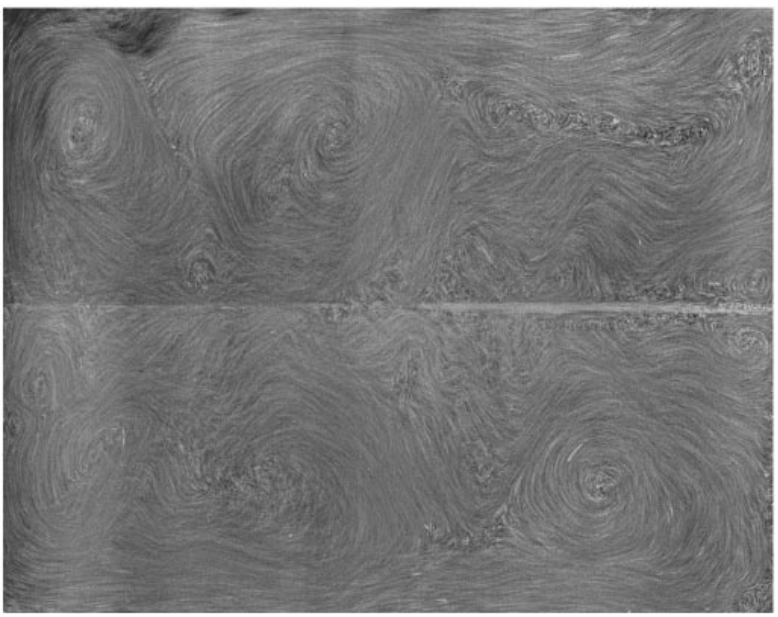

FIGURE 6. Streak photographs of a quasi-steady cycle: (*a–d*) correspond to figure 4.

region of interface increased, the buoyancy fluxes and convective velocities decreased, and the wave speed decreased. At the end of this time the characteristic thick and thin regions of the interface were no longer visible, but the interface continued to slowly seiche back-and-forth.

(*a*)

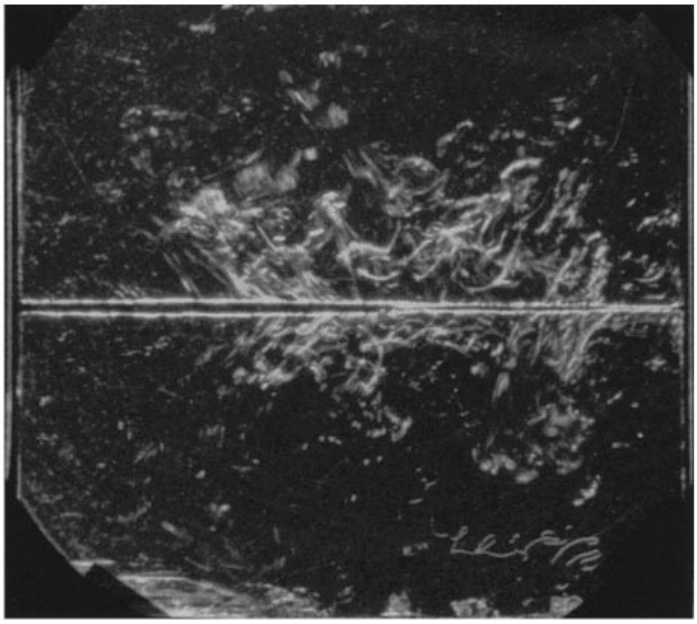

(*b*)

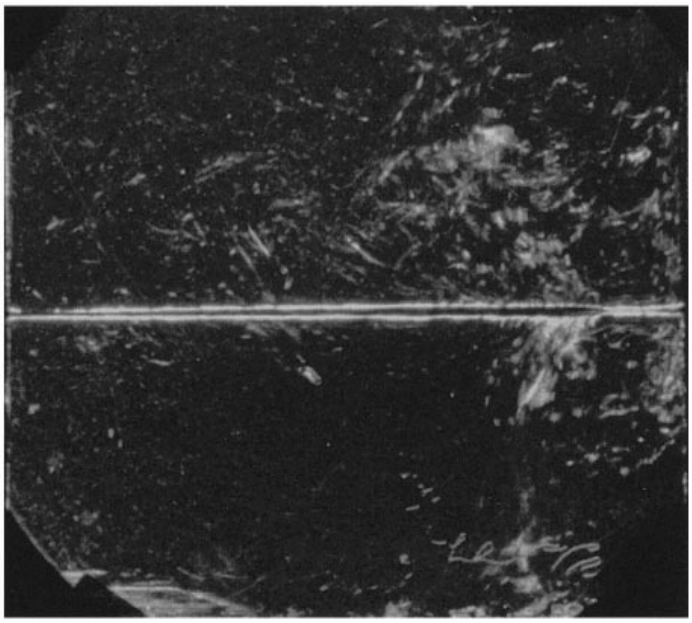

FIGURE 7(*a*, *b*). For caption see facing page.

4. Experimental plan

Both investigations made slightly different measurements of the long-term flow and it is convenient to divide the resulting experiments into two sets. The first set consists of experiments designed to ascertain the dependence of the flow on $\alpha\Delta T$ and R_ρ, for which a single channel geometry and different initial solute concentrations were used.

(*c*)

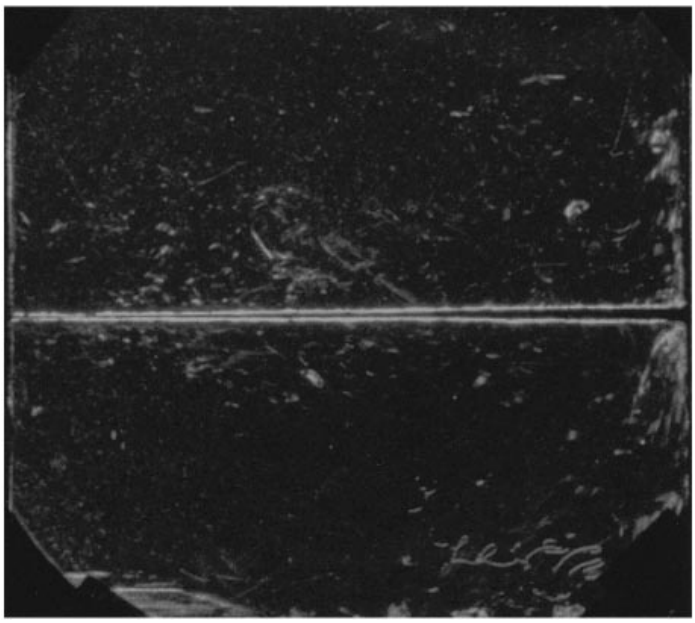

(*d*)

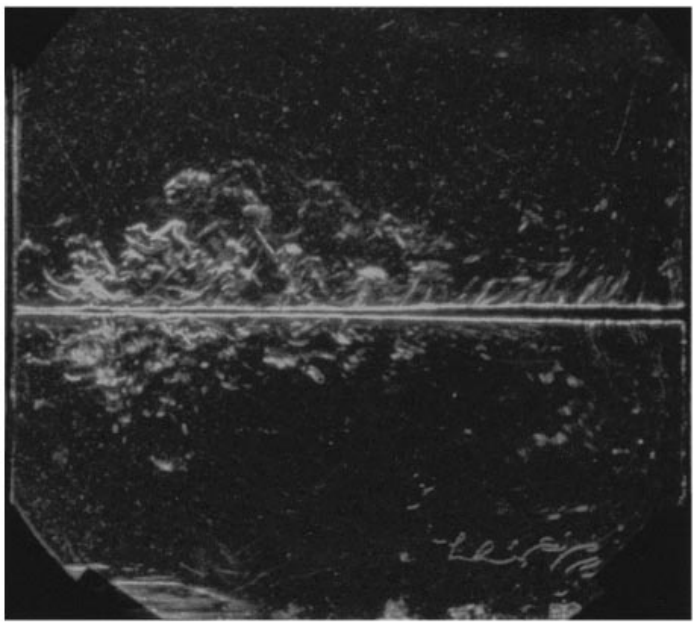

FIGURE 7. Schlieren photographs of a quasi-steady cycle: (*a–d*) correspond to figure 4.

These experiments were carried out using different cell geometries (tables 1 and 2). In addition, six experiments, each started with the same solute concentrations, were carried out at ANU in channels with horizontal cross-sections ranging from 15×5 to 180×15 cm, allowing the dependence of the flow on the channel aspect ratio L/H to be examined (table 3).

		Initial conditions		Onset of coupling			Final measurements		
Run	Symbol	$\overline{\alpha}\Delta T$	R_ρ	t (h : m : s)	$\overline{\alpha}\Delta T$	R_ρ	t (h : m : s)	$\overline{\alpha}\Delta T$	R_ρ
ANU1.1	◇	0.0279	1.05	1 : 01 : 58	0.0216	1.16	4 : 36 : 54	0.0165	1.32
ANU1.2	△	0.0348	1.04	1 : 04 : 44	0.0262	1.16	4 : 21 : 09	0.0205	1.32
ANU1.3*a*	◯	0.0462	1.03	0 : 50 : 58	0.0356	1.14	4 : 49 : 46	0.0258	1.34
ANU1.3*b*		0.0383	1.10	0 : 28 : 10	0.0345	1.15	3 : 51 : 24	0.0257	1.33
ANU1.3*c*		0.0321	1.19	0 : 10 : 20	0.0316	1.21	1 : 52 : 06	0.0279	1.30
ANU1.4	□	0.0543	1.02	0 : 53 : 18	0.0404	1.14	4 : 28 : 06	0.0294	1.33
ANU1.5	▽	0.0688	1.02	0 : 50 : 06	0.0512	1.14	4 : 03 : 21	0.0391	1.30
ANU1.6*a*†	×	0.0975	1.02	0 : 50 : 18	0.0706	1.16	4 : 02 : 36		
ANU1.6*b*‡	+	0.0975	1.02	0 : 55 : 06	0.0714	1.15	4 : 01 : 52		
ANU1.7	⊙	0.1256	1.02	1 : 00 : 04	0.0918	1.14	4 : 24 : 30	0.0703	1.30

† final samples contaminated
‡ layers added in reverse order

TABLE 1. Experimental parameters and results for the ANU experiments designed to ascertain the dependence of the flow on $\alpha\Delta T$ and R_ρ. All experiments were carried out in a 15×5 cm channel with layers of depth 11.5 cm. Experiments 1.1–1.3*a*, 1.4–1.7 were started with the widest possible range of $\alpha\Delta T$ values while maintaining R_ρ near unity. This range was limited by the practical difficulties associated with creating an interface between layers of almost equal density and the finite solubility of salt. Experiments 1.3*b, c* were started at larger R_ρ and with $\alpha\Delta T$ values such that they evolved along the same $(\alpha\Delta T, R_\rho)$ curve as experiment 1.3*a*. For each experiment the time at which a single wave formed was noted, and the corresponding values of the independent parameters inferred from the measured values at nearby times.

		Initial conditions		Final measurements		
Run	Symbol	$\overline{\alpha}\Delta T$	R_ρ	t (h : m : s)	$\overline{\alpha}\Delta T$	R_ρ
UA1*a*†	×	0.0100	1.12	20 : 40 : 45	0.0051	1.58
UA1*b*†	+	0.0104	1.12	5 : 58 : 22	0.0073	1.32
UA1*c*†‡	•	0.0099	1.13	20 : 40 : 45	0.0049	1.64
UA2†	◇	0.0100	1.21	20 : 40 : 45	0.0058	1.66
UA3†	△	0.0101	1.30	20 : 40 : 45	0.0063	1.69
UA4	◯	0.0324	1.09	6 : 47 : 22	0.0197	1.36
UA5	□	0.0325	1.14	20 : 40 : 45	0.0173	1.59
UA6	▽	0.0330	1.20	20 : 40 : 45	0.0181	1.68
UA7	⊙	0.0331	1.30	23 : 27 : 25	0.0208	1.73
UA8	⊡	0.0330	1.40	20 : 40 : 45	0.0233	1.74

† density and conductivity measured in upper layer
‡ different mode of convection

TABLE 2. Experimental parameters and results for the UA experiments designed to ascertain the dependence of the flow on $\alpha\Delta T$ and R_ρ. All experiments were carried out in a 25×10 cm channel with layers of depth 12.0 cm.

The long-term flow consisted of a single wave which propagated back-and-forth along the channel, organizing the convection in each layer into two cells which oscillated in length from zero to the full length of the channel (figure 4). Attempts to determine the convective velocities were unsuccessful with, for example, the large refractive index variations negating laser Doppler anemometry, the flow velocities being too small for hot wires and the layer densities changing too quickly for particle tracking. Indeed, had these techniques worked, it would still remain to distinguish

				Onset of coupling			Final measurements		
Run	Symbol	$L \times w$	L/H	t (h : m : s)	$\overline{\alpha}\Delta T$	R_ρ	t (h : m : s)	$\overline{\alpha}\Delta T$	R_ρ
ANU2.1	□	15×5	1.3	0 : 53 : 18	0.0404	1.14	4 : 28 : 06	0.0294	1.33
ANU2.2	△	30×5	2.6	0 : 52 : 59	0.0399	1.13	5 : 18 : 54	0.0297	1.31
ANU2.3	◯	40×5	3.5	1 : 08 : 10	0.0347	1.18	4 : 29 : 03	0.0264	1.35
ANU2.4	◇	75×15	6.5	1 : 26 : 24	0.0340	1.20	3 : 22 : 59	0.0289	1.29
ANU2.5	▽	90×15	7.8	1 : 54 : 59	0.0350	1.21	4 : 56 : 05	0.0299	1.31
ANU2.6	×	180×15	15.6	2 : 16 : 21	0.0348	1.22	5 : 31 : 53	0.0298	1.32

TABLE 3. Experimental parameters and results for the ANU experiments designed to ascertain the dependence of the flow on the channel aspect ratio, L/H. These experiments were carried out in channels with different horizontal cross-sections and started with the same solute concentrations; $\overline{\alpha}\Delta T = 0.0543$ and $R_\rho = 1.02$.

the long-time-scale motions associated with the large-scale circulations from the short-time-scale motions associated with the plumes.

The difficulties associated with determining the convective velocities forced both studies to focus on the wave behaviour. A complete description of the wave required measurements to be made several times each cycle. This approach was not practical, however, because the ANU measurements were made in real time and the UA video images did not resolve the detailed structure of the interface. Nevertheless, irregular measurements were made of the wave position. The waves were also characterized by the thickness of the thin interface, $2h$, the thickness of the thick interface, $2h_*$, and the length of the thick region, λ (refer to §5.2). Measurements of these length scales were not possible at high R_ρ because the thick and thin regions of the interface became less distinct during run-down. In addition, at low R_ρ the thin interface was observed to be < 1 mm thick, but it was not possible to determine the exact thickness because direct visualization was impaired by refractive index variations and conductivity profiles lacked sufficient spatial resolution.

4.1. *Wave measurements – The Australian National University*

In these experiments the times at which the wave (nose) reached the endwalls were noted, and, for flows carried out in long channels, position–time measurements were made while the wave propagated along the channel. Although the three-dimensional structure of the wave complicated measurements, the time at which the wave reached a given position was measured to within ± 2.5 s at low R_ρ and ± 5 s at high R_ρ. However, it was difficult to measure the nose position while the wave was banked up against an endwall, and thus the position–time measurements were generally restricted to the remaining two-thirds of the cycle.

To determine the dependence of the wave speed on the layer properties and channel dimensions, the long-time-scale behaviour had to be distinguished from the short-time-scale variations. For each experiment the 'time-dependent average wave speeds' were calculated by taking the derivative of the second-degree polynomial that best fits the displacement–time measurements, i.e. $\mathrm{d}X(t)/\mathrm{d}t$ where $X(t) = A_0 + A_1 t + A_2 t^2$. This procedure produced an analytic expression for the wave speed, which allowed values to be conveniently calculated at times when the independent parameters were known, and the resulting estimates agreed with difference estimates (refer to §5.2).

4.2. *Wave measurements – University of Auckland*

Short segments of these experiments were recorded on video, and, without the difficulties associated with real-time measurements, time and wavelength measurements were made when the wave was fully banked-up against the channel endwalls. The times were measured to within ± 5 s at low R_ρ and ± 10 s at high R_ρ, and wavelengths to ± 0.5 cm and ± 2 cm, respectively. Average values of the wave speed and wavelength were then calculated for each video segment using a minimum of five measurements.

5. Results: wave–convection coupling

5.1. *Onset of wave–convection coupling*

For each ANU experiment the time at which a single wave formed was noted, and the corresponding values of the independent and dependent parameters inferred from the measured values at nearby times. Figure 8(a, b) shows the evolution of $\alpha\Delta T$ and R_ρ for the experiments carried out in the 15×5 cm channel, with the conditions at the onset of coupling in bold. The measurements indicate that for coupling to occur the density-anomaly ratio must exceed the critical value

$$R_\rho^c = 1.15 \pm 0.01 \quad \text{for} \quad 0.0279 \leqslant (\bar{\alpha}\Delta T)_0 \leqslant 0.1256, \tag{6}$$

irrespective of the elapsed time (e.g. experiment ANU1.3b), and when flows were started above this critical value coupling started immediately (e.g. experiment ANU1.3c); table 1.

A physical argument supporting the concept of a critical density-anomaly ratio for the onset of coupling can be made by assuming that the wave speed and horizontal convective velocities must be similar for effective coupling. At the start of an experiment the buoyancy flux and resulting convective velocities are large because the interface is thin. Consequently, the wave amplitudes and speeds are too small to couple with the convective flow. However, as the system runs down the interface thickens, thereby supporting larger, and faster, waves. The resulting horizontal variations in the buoyancy flux are large enough to organize the convection into tank-scale circulations. At the same time the buoyancy flux and convective velocities decrease. Eventually the wave speeds are fast enough and the convective velocities are slow enough for coupling to occur. Since the wave amplitude and convective velocities are both controlled by the interface thickness, and this is a strong function of R_ρ, it is expected that a critical value of R_ρ must be exceeded before coupling can occur.

5.2. *Wave speed*

An important property of the waves is their speed of propagation. Figure 9 shows the time taken by the wave to travel the channel length (i.e. the half-period of the wave motion, θ) for the duration of one ANU1 experiment. The wave persisted for about 4 hours and travelled 20 m, whereas similar waves without convection only exist for 2 minutes and travel 3 m (Stamp & Jacka 1995). In addition, the half-period did not increase monotonically, but instead, while the average time taken by the wave to travel the channel length increased from 95 to 115 s, there were large (± 15 s) deviations from average values. This behaviour indicates that the wave gained energy from the convection, and, while the decrease in convective activity produced a long-time-scale decrease in wave speed, the complex wave–convection coupling dynamics produced short-time-scale variations.

In all experiments the short-time-scale variations appeared random. However,

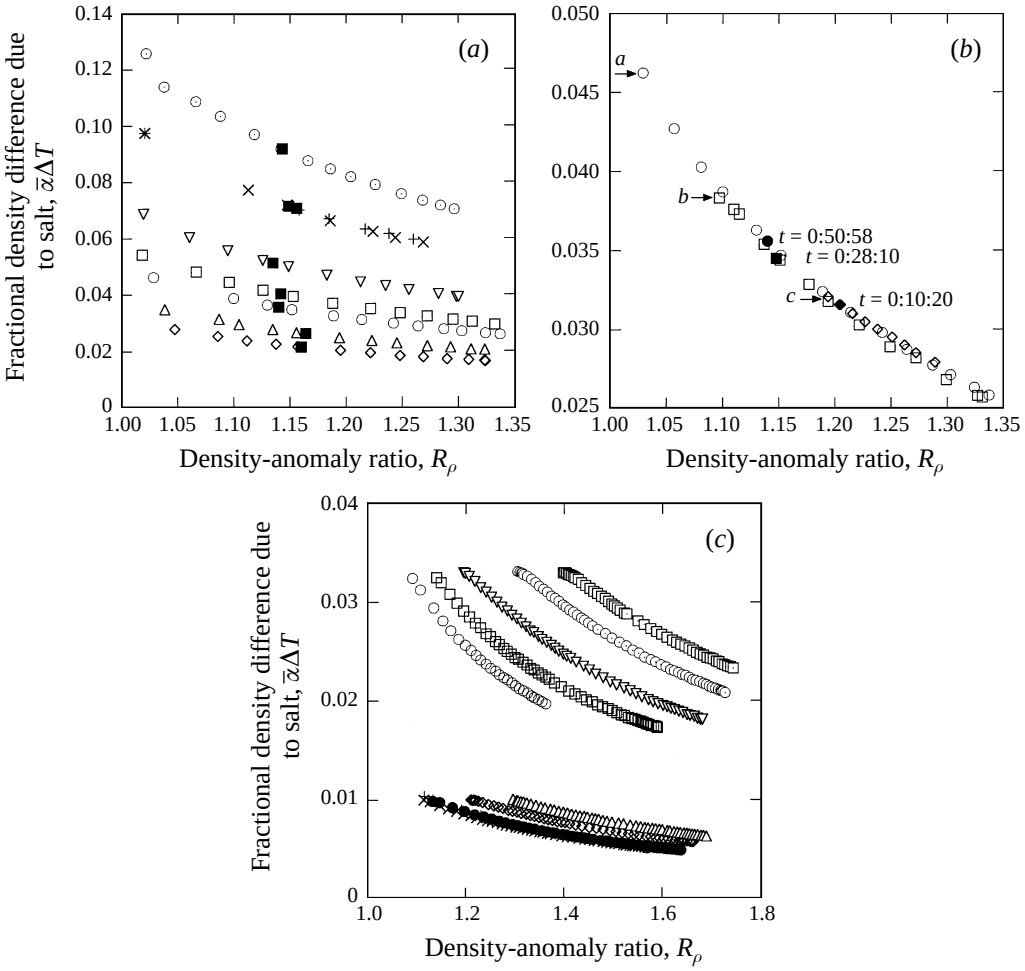

FIGURE 8. $\bar{\alpha}\Delta T$ *vs.* R_ρ for the first set of experiments. (*a*) Experiments ANU1.1–1.3*a*, 1.4–1.7, (*b*) ANU1.3*a* (○), 1.3*b* (□) and 1.3*c* (◇), and (*c*) UA1-8. The conditions at the onset of coupling are shown in bold in (*a, b*), and indicate that coupling occurred once the density-anomaly ratio exceeded the critical value $R_\rho^c = 1.15$, irrespective of the elapsed time (e.g. experiment ANU1.3*b*), and when experiments were started above this critical value coupling started immediately (e.g. experiment ANU1.3*c*). For symbols see tables 1 and 2.

because measurements were made at irregular intervals, the standard techniques for analysis of time-series data could not be used, and thus it was not possible to ascertain whether these variations resulted from random noise or deterministic chaos. Nevertheless, two factors which may have caused the variations were identified. First, small three-dimensional convection cells were observed along the thin interface ahead of the wave, and as these cells moved randomly about, expanding, contracting and merging, the conditions experienced by the wave changed. Second, small thick regions of interface occasionally formed along the otherwise thin interface ahead of the wave, and the wave may have suffered a phase shift on colliding with these lumps (Stamp & Jacka 1995).

Figure 10(*a*) shows the average wave speed for each ANU1 experiment plotted against the density-anomaly ratio. Two features emerge. First, during the lifetime of

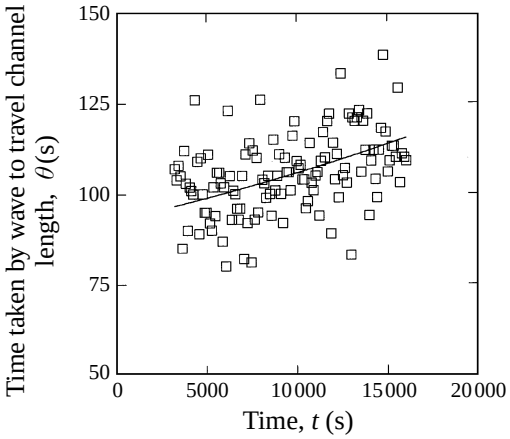

FIGURE 9. Half-period of wave motion *vs.* time since the start of the experiment. The average time taken to travel the channel length (———) increased from 95 to 115 s as the convection weakened; however, the complex wave–convection coupling dynamics produced large (±15 s) fluctuations (□). For each ANU experiment the average wave speeds were determined from the derivative of the second-degree polynomial that best fits the displacement–time measurements, $\mathrm{d}X(t)/\mathrm{d}t$ where $X(t) = A_0 + A_1 t + A_2 t^2$.

each wave, $\alpha\Delta T$ decreased two-fold, R_ρ increased from 1.15 to 1.40, and in response the wave speed decreased by about 20%. Second, each flow occupied a different region of parameter space, with flows started with larger $\alpha\Delta T$ values having faster waves. Thus the wave speed was largest when the interfacial density difference due to salt ($\alpha\Delta T$) was large and the stability of the interface was low ($R_\rho \to 1$), that is, when the fluxes were largest. However, whilst there was an order of magnitude difference in the fluxes during experiments ANU1.1 and 1.7 (i.e. $(\alpha\Delta T)_0 = 0.0279$ and 0.1256), the fact that wave speeds in the latter, more active, flow were only about twice those in experiment ANU1.1 indicates that the wave speed was weakly dependent on the flux. Similar behaviour is observed for the UA experiments, although the trends are less distinct than those of the ANU experiments (figure 10*c*). This difference probably occurs because the UA wave speeds were calculated by averaging over several cycles and this method is susceptible to errors due to the large short-time-scale variations.

To examine this behaviour in a more rigorous fashion, the argument used to explain the concept of a critical density-anomaly ratio for the onset of coupling was made more quantitative. Consider a flow in which a wave propagates along a channel assisted by a tank-scale convection cell in each layer (figure 11). The wave is thick enough to turn off the local interfacial fluxes, and thereby gives rise to tank-scale density gradients which organize the convection over the channel length. Hence the horizontal convective velocities are given by

$$u \sim (g\delta\rho H/\rho_0)^{1/2}, \tag{7}$$

where $\delta\rho$ is the horizontal density difference along each layer and ρ_0 is a reference density. In the special, unattainable, case of a steady balance between the interfacial flux and horizontal advection,

$$F \sim u\delta\rho H/\gamma L, \tag{8}$$

where F is the mass flux (i.e. units $\mathrm{g\,cm^{-2}\,s^{-1}}$) through the thin interface ahead of the

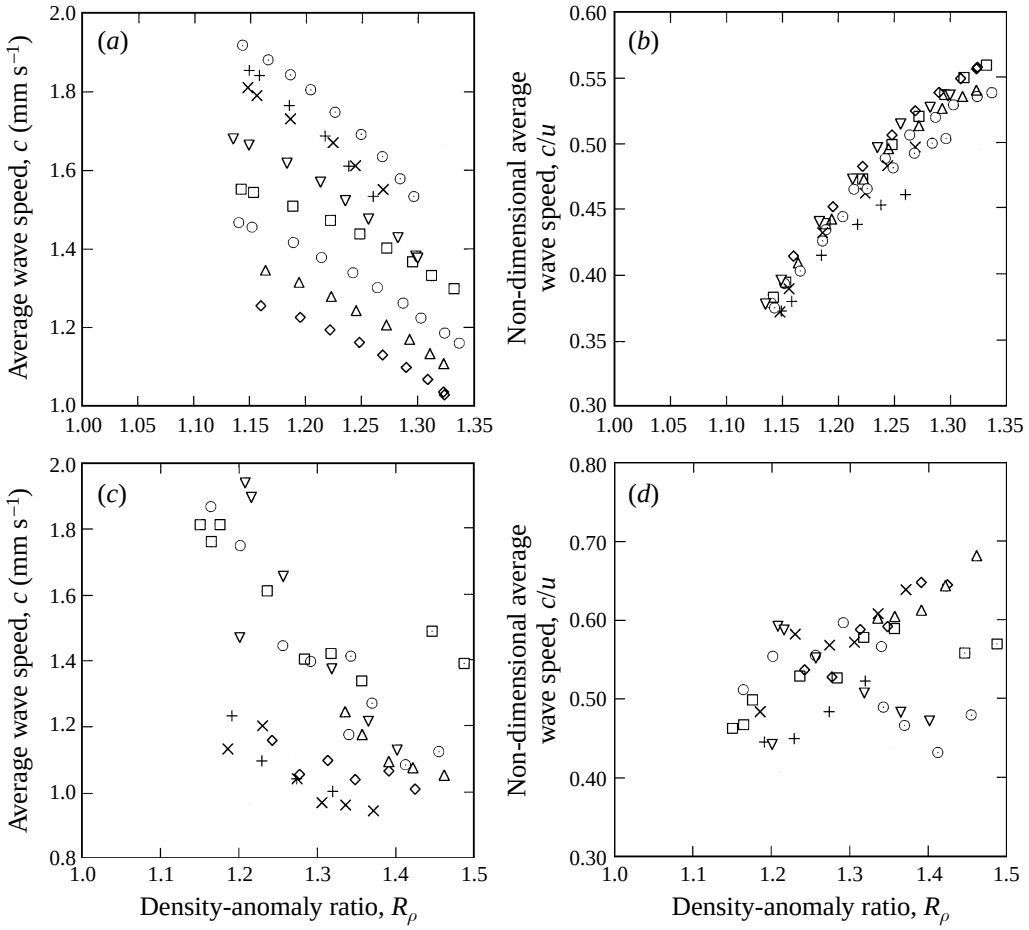

FIGURE 10. Wave speed results for the ANU1 (a, b) and UA (c, d) experiments. (a, c) c *vs.* R_ρ. The wave speed was largest when the interfacial density difference due to salt ($\propto \Delta T$) was large and the stability of the interface was low ($R_\rho \to 1$). (b, d) c/u *vs.* R_ρ, where the horizontal convective velocities are assumed to be proportional to $(BL)^{1/3}$. Non-dimensionalizing the wave speeds for each experiment by this velocity collapses all the measurements onto the same curve, and this confirms that coupling requires a matching of the wave and convection speeds. The increase in c/u with increasing R_ρ suggests that the exact nature of the coupling depends on the structure of the interface.

wave, which occupies a proportion γ of the total interfacial area. Rearranging gives

$$u \sim (b\gamma L)^{1/3}, \tag{9}$$

where $b = gF/\rho_0$ is the equivalent buoyancy flux (i.e. units $\mathrm{cm^2\,s^{-3}}$). Thus the usual relationship between the convective velocities and buoyancy flux (i.e. $u \sim (bH)^{1/3}$, Hunt 1984) applies, despite the fact that the convection is organized over the channel length. Now consider the wave. Stamp & Jacka (1995) showed that the speed of large-amplitude solitary waves propagating along a slightly diffused density interface between two deep motionless layers of constant density is given by

$$c = (gh\Delta\rho/\rho_0)^{1/2} f(a/h), \tag{10}$$

where the amplitude function $f(a/h) \sim a/h$ for $a/h \gg 1$. If coupling requires that

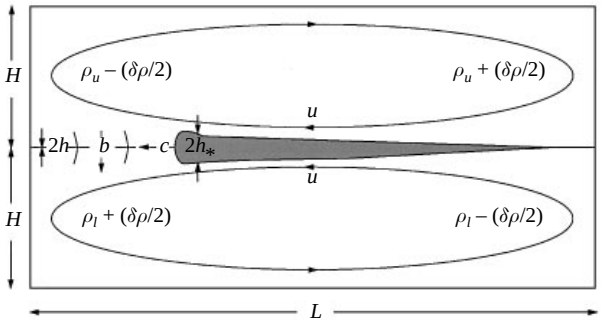

FIGURE 11. Wave–convection coupling model. A wave propagates along a channel, with the convection organized over the channel length by the tank-scale density gradients resulting from the horizontal variations in the interfacial buoyancy flux. The model assumes that the wave selects an amplitude such that its speed is similar to the horizontal convective velocities (i.e. $c \sim u$), with analytical results derived for the case of a steady balance between the interfacial flux and horizontal advection.

the wave speed and horizontal convective velocities are similar (i.e. $c \sim u$), then for $a/h \gg 1$, the amplitude selected by the wave is

$$a/h \sim (gh\Delta\rho/\rho_0)^{-1/2}(b\gamma L)^{1/3}, \tag{11}$$

and this closes the argument.

The experimental measurements presented in §6 show that the average interfacial buoyancy flux was given by $B \approx B_*(\alpha\Delta T)^{4/3}F_T^*(R_\rho,\tau)(1-\tau^{1/2})^{1/3}$, where $B_* = 0.085(g^4\kappa_T^2/\nu)^{1/3}$ is a constant with units $\mathrm{cm^2\,s^{-3}}$, and, although the flux b through the thin interface ahead of the wave was greater than B, it is reasonable to expect that b scaled with the average value (i.e. $b\gamma L = BL$). Thus the wave amplitude and speed can be expressed in terms of the independent parameters:

$$\begin{aligned} a/h &\sim (gh\Delta\rho/\rho_0)^{-1/2}(BL)^{1/3} \\ &\sim [(B_*L)^{1/3}/(gh)^{1/2}](\alpha\Delta T)^{-1/18}(R_\rho-1)^{-1/2}F_T^{*1/3}(1-\tau^{1/2})^{1/3}, \qquad (12a) \\ c &\sim (BL)^{1/3} \sim (B_*L)^{1/3}(\alpha\Delta T)^{4/9}F_T^{*1/3}(1-\tau^{1/2})^{1/3}, \qquad (12b) \end{aligned}$$

where $\Delta\rho/\rho_0 \equiv \beta\Delta S - \alpha\Delta T \equiv \alpha\Delta T(R_\rho - 1)$ has been used and the thickness of the thin interface ahead of the wave, $h(\alpha\Delta T, R_\rho)$, is left as an unspecified function.

Although these results were derived without a detailed knowledge of the wave, and variations in the wave and convective motions during each cycle are ignored, they reproduce two fundamental features of the flow. First, with both experiments and Linden & Shirtcliffe's (1978) model suggesting that the thickness of the interface is most strongly affected by R_ρ, (12*a*) shows that the wave amplitude is weakly dependent on $\alpha\Delta T$ and strongly dependent on R_ρ as, from §6, $F_T^* \sim {R_\rho}^{-5.6}$. This result is consistent with the observation that the various flow regimes started at critical values of R_ρ. Second, non-dimensionalizing the wave speeds for each experiment by the horizontal convective velocities (9) collapses all the measurements onto a single curve, and this is consistent with the wave speed being proportional to $(\alpha\Delta T)^{4/9}$ (figure 10*b*, *d*). However, during each experiment the wave speed decreased more slowly than the horizontal convective velocities, and thus c/u increased with increasing R_ρ. The wave and the convective motions were observed to be coupled for $0.39 \leqslant c/u \leqslant 0.54$ (figure 10*b*), suggesting that the exact nature of the coupling depends on the structure of the interface, which is a strong function of R_ρ. Indeed, it is unfortunate that the

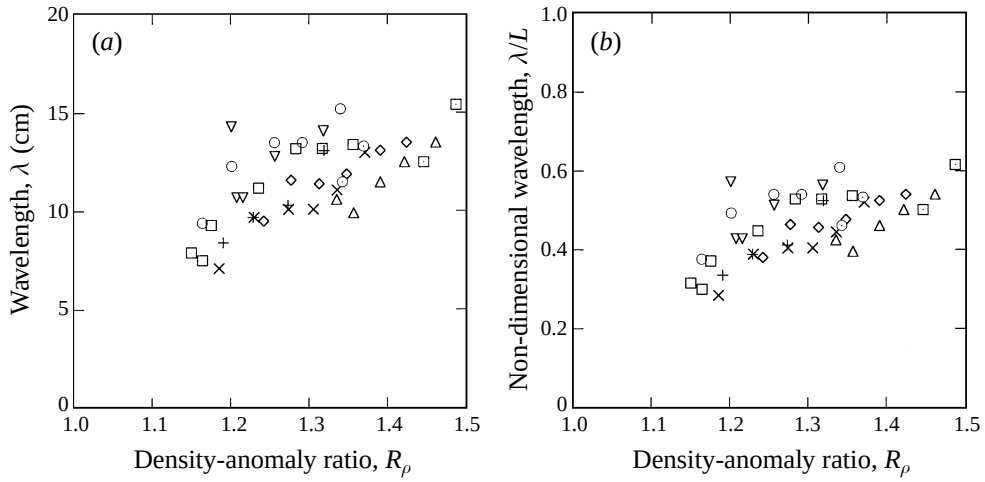

FIGURE 12. Wavelength results for the UA experiments: (*a*) λ *vs.* R_ρ, (*b*) λ/L *vs.* R_ρ. The wavelength increases with increasing R_ρ; however, the experimental scatter does not allow a dependence on $\alpha\Delta T$ to be identified.

thickness of the interface could not be measured because without such measurements the expression derived for the wave amplitude (12*a*) cannot be tested.

5.3. *Wavelength*

Figure 12 shows the wavelength for each UA experiment plotted against the density-anomaly ratio, and, as observed during experiments carried out in different channels, values range between 25% and 60% of the channel length. The experimental scatter does not allow a dependence on $\alpha\Delta T$ to be identified; however, the wavelength clearly increases with increasing R_ρ. This behaviour is consistent with the prediction of the steady-state resonance model that the flow primarily depends on the density-anomaly ratio, and occurs because at large R_ρ the weak convection cannot sweep as much interfacial fluid against the channel endwall.

5.4. *Effects of the channel aspect ratio*

The same qualitative behaviour occurred in both short (15 cm) and long (180 cm) channels; however, as expected, there were quantitative differences between these flows. For example, in the latter case the convection cells were long and flat ($L/H = 15.6$), and the wave took about 10 minutes to travel the channel length.

Figure 13 shows the evolution of $\alpha\Delta T$ and R_ρ for the second set of ANU experiments, and, with the conditions at the onset of coupling in bold, indicates that the critical value of R_ρ for coupling increased as the channel length increased. This behaviour occurred because, by (9), a longer channel leads to larger horizontal convective velocities once the convection becomes organized over the channel length, which in turn demands a greater interfacial wave speed for coupling. However, these larger wave speeds cannot occur until the interface is thicker than it is at the onset of coupling in shorter channels, and therefore the critical value of R_ρ is greater.

This argument is further supported by the fact that when the channel length increased from 15 to 180 cm, the wave speed increased by a factor of two, i.e. compare experiments ANU2.1 and 2.6. Indeed, this dependence was successfully predicted by the $c \propto (BL)^{1/3}$ result derived from the steady-state resonance model (figure 14).

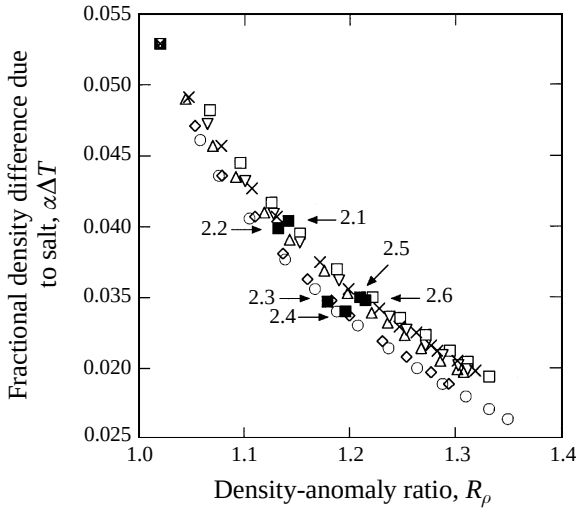

FIGURE 13. $\bar{\alpha}\Delta T$ *vs.* R_ρ for the second set of ANU experiments (see table 3). The conditions at the onset of coupling are in bold and indicate that the critical value of R_ρ for coupling increased as the channel length increased.

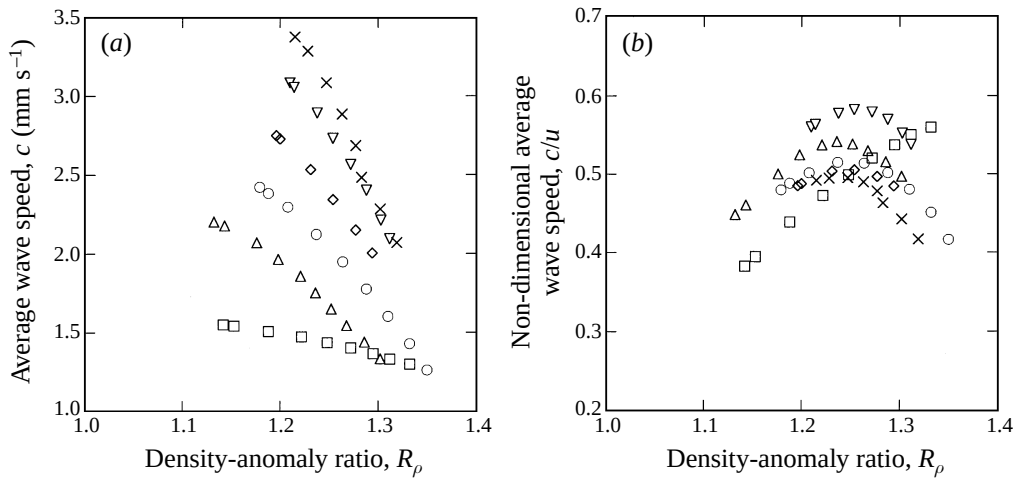

FIGURE 14. Wave speed results for the second set of ANU experiments. (*a*) c *vs.* R_ρ. To allow direct comparison between experiments, the flows were started with the same $\alpha\Delta T$ and R_ρ, and hence the plot indicates that the wave speed increased with increasing channel length. (*b*) c/u *vs.* R_ρ. The collapse of the data indicates that the wave speeds are proportional to $(BL)^{1/3}$.

6. Results: interfacial fluxes

In this section the measured fluxes are presented and compared with previous experimental measurements and theoretical predictions.

6.1. *Definitions*

The fluxes across a diffusive interface can be determined by measuring the rate of change of the properties in the adjacent layers or by measuring the gradients through the interface and using the known molecular diffusivities of the two components to calculate the diffusive fluxes through the core. However, even in regimes where

the diffusive fluxes through the core are equal to the convective fluxes from the boundary layers, the validity of the second method is questionable because the present experiments indicate that there are often significant horizontal variations in the thickness of the interface. Thus the fluxes were determined from the layer properties.

McDougall (1981*a, b*) discussed the conservation equations for two-layer systems and noted that, in general, given interfacial T and S mass fluxes produce different buoyancy fluxes into the upper and lower layers. However, it was not possible to resolve differences between the buoyancy fluxes into the upper and lower layers; there were no discernible differences in the convective motions in the layers and the interface position remained unchanged to within ± 0.5 mm during each experiment. It was therefore appropriate to use the average buoyancy flux

$$\overline{B} \approx \left(\frac{gH}{2}\right)\frac{\mathrm{d}}{\mathrm{d}t}\left(\frac{\Delta\rho}{\rho_0}\right) = -\left(\frac{gH}{2}\right)\frac{\mathrm{d}}{\mathrm{d}t}(\overline{\alpha}\Delta T - \overline{\beta}\Delta S) = -\left(\frac{gH}{2}\right)\left[\frac{\mathrm{d}}{\mathrm{d}t}(\overline{\alpha}\Delta T)\right](1-\overline{R}_f), \tag{13}$$

where $\Delta\rho/\rho_0 \equiv \overline{\beta}\Delta S - \overline{\alpha}\Delta T$ has been used, and

$$\overline{R}_f \approx \frac{\mathrm{d}(\overline{\beta}\Delta S)/\mathrm{d}t}{\mathrm{d}(\overline{\alpha}\Delta T)/\mathrm{d}t} = \frac{\mathrm{d}(\overline{\beta}\Delta S)}{\mathrm{d}(\overline{\alpha}\Delta T)} \tag{14}$$

is the ratio of the T and S contributions to the average buoyancy flux. Thus the buoyancy flux was proportional to the rate of change of $\Delta\rho/\rho_0$, and the T and S contributions were proportional to the rate of change of $\overline{\alpha}\Delta T$ and $\overline{\beta}\Delta S$, respectively.

6.2. *Salt* (T) *flux*

To calculate the salt flux it was necessary to differentiate the measured $\alpha\Delta T$ values with respect to time. Following Shirtcliffe (1973), the function

$$\alpha\Delta T \propto \left(\frac{t}{t_0} - 1\right)^{-\gamma} \tag{15}$$

was fitted to the data for each experiment and flux values calculated from differentiating the fit. This procedure had two advantages over difference estimates. First, the procedure was insensitive to errors in point values of $\alpha\Delta T$ because the fit was a smooth representation of the data. Second, the derivation of an analytic expression for the flux allowed values to be conveniently calculated at times when the independent parameters were known. However, smoothing the data in this manner resulted in poor flux estimates at the start and end of each experiment, with the first and last estimates having to be eliminated from the analysis. In all experiments the flux estimates calculated from a difference formula and the curve fit agreed within expected uncertainties (figure 15).

Figure 16(*a*) shows the salt flux for each ANU1 experiment plotted against the density-anomaly ratio. As expected, the flux was largest when the interfacial density difference due to salt ($\alpha\Delta T$) was large and the stability of the interface was low ($R_\rho \to 1$). Turner (1965) used dimensional arguments to suggest that this dependence takes the form

$$\alpha F_T = 0.085\rho(g\kappa_T^2/\nu)^{1/3}(\alpha\Delta T)^{4/3}F_T^*(R_\rho, \tau), \tag{16}$$

where $F_T^*(R_\rho, \tau)$ must be determined experimentally and is the ratio of the measured flux to that if the interface were replaced by a 'solid plane' that conducts T but is impermeable to S. The dependence of the fluid properties on the salt and sugar

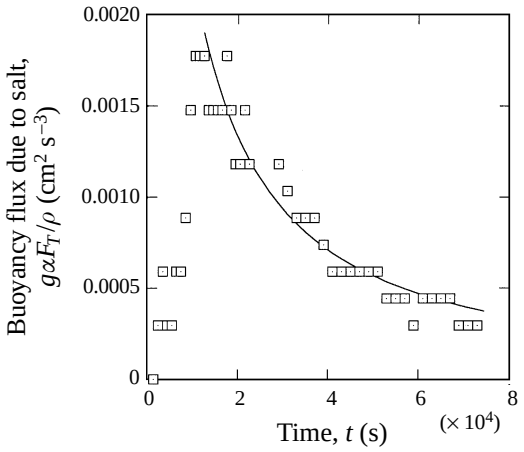

FIGURE 15. Salt (T) flux estimates, $(gH/2)\ \mathrm{d}(\bar{\alpha}\Delta T)/\mathrm{d}t$, determined from a difference formula (⊡) and the derivative of the power law $\bar{\alpha}\Delta T \propto (t/t_0 - 1)^{-\gamma}$ that best fits the data (———). In this experiment significant mixing occurred while filling and, as seen from the anomalously low fluxes at the start of the experiment, a period of inactivity followed. The initial data were therefore ignored, with the subsequent curve fit producing a smooth representation of the remaining data and allowing fluxes to be conveniently calculated at times when the independent parameters were known.

concentrations was taken into account while evaluating F_T^*, with the main effect being to increase the viscosity of the lower (sugar) layer. As suggested by Shirtcliffe (1973), the ν value for each experiment was taken as that of a sugar solution whose density increment over pure water was 75% of the increment of the sugar solution used to start the experiment. The coefficient of diffusion for salt (units cm^2 s^{-1}) was then calculated as $1.2 \times 10^{-7}/\mu$ where μ is the corresponding dynamic viscosity (units g cm^{-1} s^{-1}).

The resulting F_T^* values for the ANU1 and UA experiments, as well as those supplied by Shirtcliffe, are shown in figure 16(*b–d*).† Formal error analysis suggests that the current experimental values have uncertainties of about 10% at $R_\rho \approx 1$ and less than 50% at the largest R_ρ, but the experimental data exhibit a precision an order of magnitude smaller. Shirtcliffe's (1973) values have uncertainties "that should not exceed 50% at $R_\rho \approx 1$ and somewhat more when $R_\rho \geqslant 2$, and somewhat less in between." These large uncertainties explain the order of magnitude variations in Shirtcliffe's fluxes at low R_ρ, and possibly the fact that neither the ANU nor UA studies found salt fluxes that exceeded the solid plane value (i.e. $F_T^* > 1$) whereas Shirtcliffe (1973) did.

In all three studies the F_T^* values for the different experiments collapse onto a single curve and this is consistent with Turner's assertion that fluxes are proportional to $(\alpha\Delta T)^{4/3}$. However, small deviations in the exponent cannot be tested because of the large uncertainties in the measured fluxes, and the fact that even at low R_ρ there is less than an order of magnitude variation in the $\alpha\Delta T$ values for the different experiments. Thus additional experiments are required to test Kelley's (1990) suggestion that fluxes should be proportional to $\alpha\Delta T$ raised to a power between 5/4 and 4/3 depending on whether free or no-slip conditions hold at diffusive interfaces. Moreover, it might be expected that the wave–convection coupling could invalidate the 4/3 law. For

† In plotting the F_T^* *vs.* R_ρ data it was found that the current experimental values were quite different to Shirtcliffe's (1973) values despite the graphs of $\alpha\Delta T$ *vs.* $t - t_0$ and $\beta\Delta S$ *vs.* $\alpha\Delta T$ being similar. On subsequent inspection of his data, Dr Shirtcliffe found that an error had been made in non-dimensionalizing the measured fluxes and graciously supplied the corrected values.

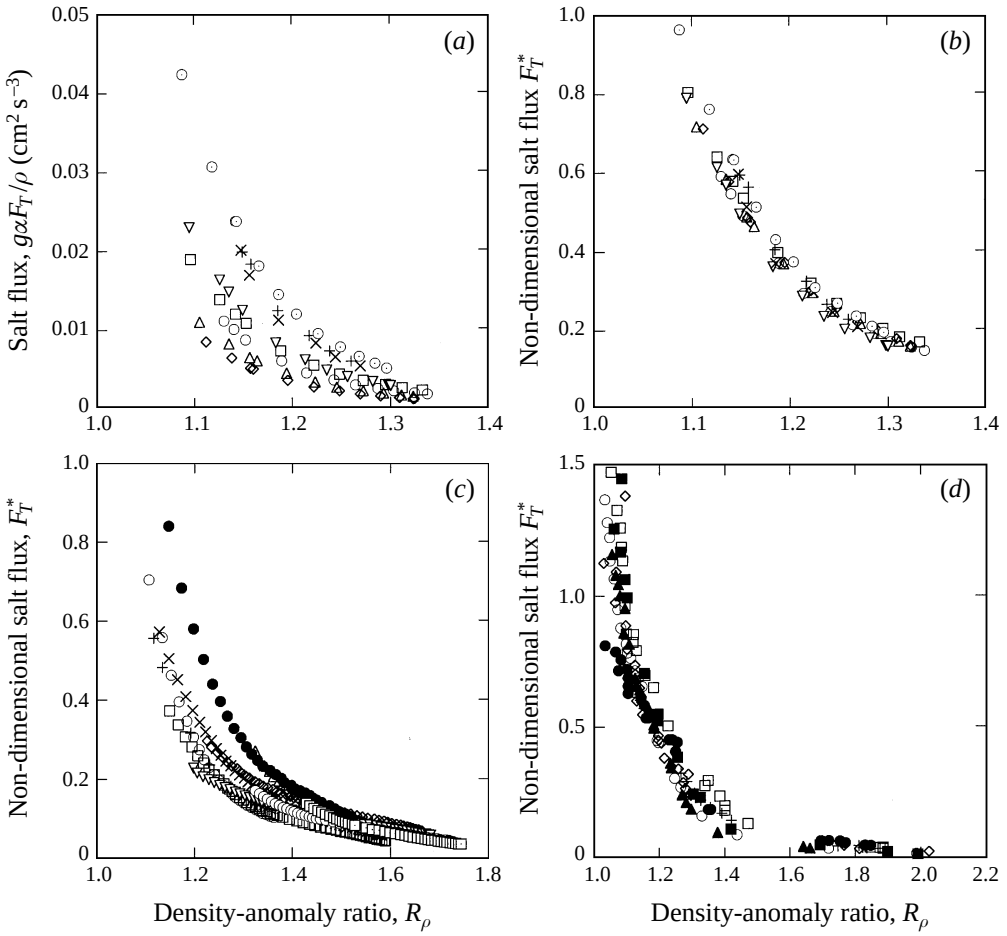

FIGURE 16. Salt (T) flux results. (*a*) $g\alpha F_T/\rho$ *vs.* R_ρ for the ANU1 experiments. As expected, the flux was largest when the interfacial density difference due to salt ($\alpha\Delta T$) was large and the stability of the interface was low ($R_\rho \to 1$). (*b–d*) F_T^* *vs.* R_ρ for the (*b*) ANU1, (*c*) UA and (*d*) Shirtcliffe's (1973) experiments. The symbols for Shirtcliffe's (1973) data are from the original: experiment 2 (+), 5 (□), 6 (◇), 7 (●), 8 (▲), 9 (■), 10 (○), with the data from the remaining experiments being unavailable. In each case the non-dimensional fluxes for the different experiments collapse onto a single curve, and this is consistent with Turner's assertion that fluxes are proportional to $(\alpha\Delta T)^{4/3}$.

example, Siggia (1994) noted that when large-scale convective circulations occur in turbulent thermal convection, the layer depth is reintroduced into the problem via the Reynolds number and the invasion of the thermal boundary layers by the turbulent shear flow driven by the largest eddies. Nevertheless, whilst it is clear that the coupling affects the boundary layers, the scaling analysis presented in § 5.2 indicates that the large-scale horizontal flow depends on the channel length rather than the layer depth, and thus the layer depth may be unimportant and the 4/3 law applicable.

For predictive purposes it is useful to parameterize the dependence of the non-dimensional salt flux on the density-anomaly ratio. The data from the three studies are plotted in figure 17(*a*), and although the three are in reasonable agreement it is clear that Shirtcliffe's (1973) values are somewhat larger than the corresponding ANU and UA values. Measurements presented in § 6.4 suggest that fluxes depend on the exact nature of the flow, and, with the flow during Shirtcliffe's (1973) experiments

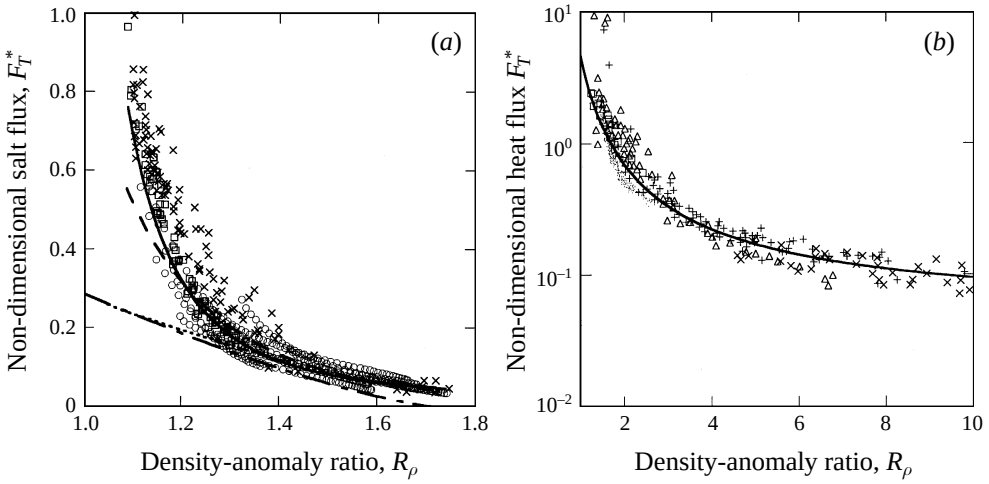

FIGURE 17. F_T^* *vs.* R_ρ. (*a*) Salt–sugar experiments: ANU1 (□), UA (○) and Shirtcliffe (1973) (×), with the unreliable data omitted. Also shown is the best fit to the ANU and UA data (———), the best power law fit (— — —), Linden & Shirtcliffe's (1978) analytical predictions (—— - ——), and the numerical predictions (·····). (*b*) Heat–salt experiments: Turner (1965) △, Crapper (1975) •, Marmorino & Caldwell (1976) +, Newell (1984) ×, and Taylor (1988) □. The solid line is the best fit to the data $F_T^* = 0.038\exp(4.8R_\rho^{-0.72})$ (Kelley 1990).

being unknown, it was decided not to include these experiments in the formulation. Experiment UA1.1*c*, which was characterized by a flow pattern consisting of two interfacial waves, was omitted for the same reason. A simple power law was then fitted to the remaining 443 data points:

$$F_T^* = 0.89R_\rho^{-5.6} \quad \text{for} \quad 1.09 \leqslant R_\rho \leqslant 1.74, \tag{17}$$

and, whilst underestimating the fluxes at low R_ρ, is used in the scaling analysis presented in § 5.2 because it is convenient and sufficiently accurate. A number of other functional forms were fitted to the data with

$$F_T^* = 0.012\exp(5.1R_\rho^{-2.4}) \quad \text{for} \quad 1.09 \leqslant R_\rho \leqslant 1.74 \tag{18}$$

providing the best overall fit.

Finally, comparison of figures 17(*a*) for the salt–sugar system and 17(*b*) for the heat–salt system shows the effect of the diffusivity ratio on the fluxes across a diffusive interface. When $\tau \approx 1/100$ F_T^* decreases by two orders of magnitude over $1 \leqslant R_\rho \leqslant 10$, whereas when $\tau \approx 1/3$ a similar decrease occurs when R_ρ increases to just 2. Moreover, the present accumulation of data does not support Shirtcliffe's suggestion that for the constant flux ratio regime the non-dimensional flux is given by $F_T^* = \psi R_\rho^\phi$, where $\psi \approx 2.3$ and ϕ is a function of the diffusivity ratio.

6.3. *Flux ratio*

Although transport across a diffusive interface is described by the T and S fluxes, results are usually presented in terms of the T flux and the ratio of the T and S fluxes. This description is preferred because T is the component that drives the convection, and the behaviour of the flux ratio indicates whether double-diffusion or turbulent mixing is the dominant transport mechanism.

Equation (14) shows that the average flux ratio can be estimated as the gradient of the graph of $\overline{\beta}\Delta S$ against $\overline{\alpha}\Delta T$. However, more accurate estimates were obtained in a

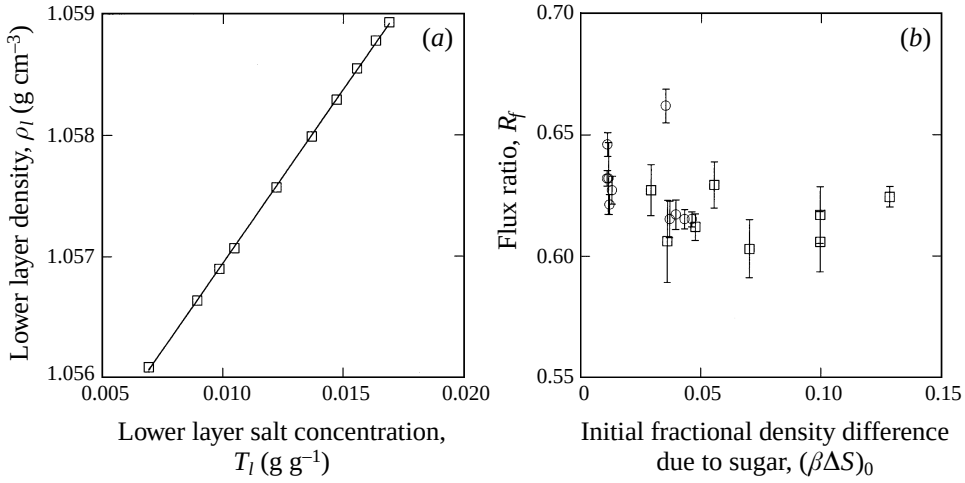

FIGURE 18. Flux ratio results. (*a*) ρ_l *vs.* T_l. The slope $\mathrm{d}\rho/\mathrm{d}T$ was constant and, because $\rho\alpha = \partial\rho/\partial T$ varied by less than 2% during the experiment, the lower layer flux ratio was also constant. (*b*) $\overline{R}_f$ *vs.* $(\overline{\beta}\Delta S)_0$ for the ANU1 (□) and UA (○) experiments. The flux ratios for each experiment were similar, $\overline{R}_f = 0.62 \pm 0.01$, which is consistent with Shirtcliffe's (1973) measurements, $R_f = 0.60 \pm 0.02$, and Linden & Shirtcliffe's (1978) prediction of $R_f = \tau^{1/2} = 0.58 \pm 0.02$ for purely double-diffusive transport.

manner analogous to that used by Griffiths & Ruddick (1980) for the finger regime. The rate of change of density in each layer is

$$\frac{\mathrm{d}\rho}{\mathrm{d}t} = \rho\alpha\frac{\partial T}{\partial t} + \rho\beta\frac{\partial S}{\partial t} = \rho\alpha\frac{\partial T}{\partial t}\left(1 - \frac{\beta}{\alpha}\frac{\mathrm{d}S}{\mathrm{d}T}\right) = \rho\alpha\frac{\partial T}{\partial t}(1 - R_f) \tag{19}$$

and, therefore,

$$(1 - R_f) = \frac{1}{\rho\alpha}\frac{\mathrm{d}\rho}{\mathrm{d}T}. \tag{20}$$

This result is true for each layer separately, and flux ratios estimated in this manner were more accurate than those estimated from (14) for two reasons. First, ρ was known with greater precision than the derived quantities $\overline{\alpha}\Delta T$ and $\overline{\beta}\Delta S$ because it was measured directly. Second, even a 10% error in the right-hand side of (20) results in only a 1% error in the flux ratio because $R_f \approx 1$.

Figure 18(*a*) shows the ρ_l *vs.* T_l data for one experiment. The slope $\mathrm{d}\rho/\mathrm{d}T$ was constant and, because $\rho\alpha = \partial\rho/\partial T$ varied by less than 2%, the lower layer flux ratio was also constant. Here an average flux ratio was appropriate, and figure 18(*b*) shows the average flux ratio for each ANU1 and UA experiment plotted against the initial fractional density difference due to sugar. Shirtcliffe (1973) found a slow increase of R_f with increasing $(\beta\Delta S)_0$ and suggested that this occurred because changes in viscosity of the fluids affect the diffusivities. However, no such trend was apparent here, and both sets of measurements are well represented by the average value

$$\overline{R}_f = 0.62 \pm 0.01 \quad \text{for} \quad 1.07 \leqslant R_\rho \leqslant 1.78. \tag{21}$$

This value is consistent with Shirtcliffe's (1973) measurements, $R_f = 0.60 \pm 0.02$, and Linden & Shirtcliffe's (1978) prediction of $R_f = \tau^{1/2} = 0.58 \pm 0.02$ for purely double-diffusive transport.

6.4. *Effects of wave–convection coupling on the fluxes*

If theoretical models of the diffusive interface are to be used for predicting fluxes in geophysical and technological settings, then it is necessary to determine whether the wave–convection coupling affects the interfacial fluxes. There are two mechanisms by which coupling could increase the fluxes. First, the gradients of T and S across the thin interface ahead of the wave were much larger than would be the case if the interface were rearranged to be of uniform thickness. Second, the large-scale convective circulations maintained these thin (high flux) regions by sweeping the interfacial fluid to the wave.

The best method of determining the effects of coupling on the fluxes is to compare fluxes measured for flows with and without coupling. However, no useful method of suppressing coupling was found. For example, placing steel wool at the channel endwalls failed to dissipate waves, and coupling occurred irrespective of the layer depths and tank geometry (Stamp & Griffiths 1997). In addition, although flows dominated by viscous dissipation at the tank sidewalls did not exhibit long-term coupling, the 15×2.5 cm channel available for such experiments did not contain enough fluid for accurate concentration measurements to be made.

Given the absence of suitable control experiments, the measured fluxes were compared with Linden & Shirtcliffe's (1978) time-independent model, which assumes that the interface is of uniform thickness and that the boundary layers grow and break away in a periodic fashion. In this manner the model predicts that

$$F_T^* = \left(\frac{1}{\pi} \frac{(1 - \tau^{1/2} R_\rho)^4}{1 - \tau^{1/2}} \right)^{1/3}, \tag{22}$$

which, as seen from figure 17(*a*), underestimates the fluxes at low R_ρ, is in reasonable agreement over the range $1.20 \leqslant R_\rho \leqslant 1.60$, and fails at high R_ρ where the steady-state assumption is invalid. Linden & Shirtcliffe (1978) observed similar behaviour and noted that in the limit $R_\rho \to 1$, the model assumptions, that the gradients through the diffusive core are constant and that the core is much thicker than the boundary layers, are violated. Thus it is necessary to check if these assumptions are violated in the experiments, and, if so, whether this could account for the large fluxes found at low R_ρ. A numerical model based on Linden & Shirtcliffe's (1978) analytical model but allowing for variable core gradients and thick boundary layers was therefore developed. The model is described in the Appendix, and indicates that, although both assumptions are violated at low R_ρ, Linden & Shirtcliffe's (1978) predictions are reasonably accurate because the core gradients they used were close to the cycle-averaged values (figure 17*a*).

Taking the numerical model as an accurate representation of a steady uniform interface it is now possible to consider the effect of the coupling on the fluxes. The numerical model underestimates the fluxes for $R_\rho < 1.13$ and, with waves not observed under these conditions, this discrepancy probably results from the redistribution of interfacial fluid by the convection (figure 3*a–d*). Over the range $1.13 \leqslant R_\rho < 1.20$ the model fluxes are again too small and this is attributed to the strong coupling. There is, however, good agreement between the measured and predicted fluxes for $R_\rho \geqslant 1.20$ despite the fact that the system supported waves under these conditions. This agreement most likely occurs because run-down results in smaller horizontal variations in the thickness of the interface and weaker large-scale circulations.

It is also useful to compare the fluxes measured for experiments having different

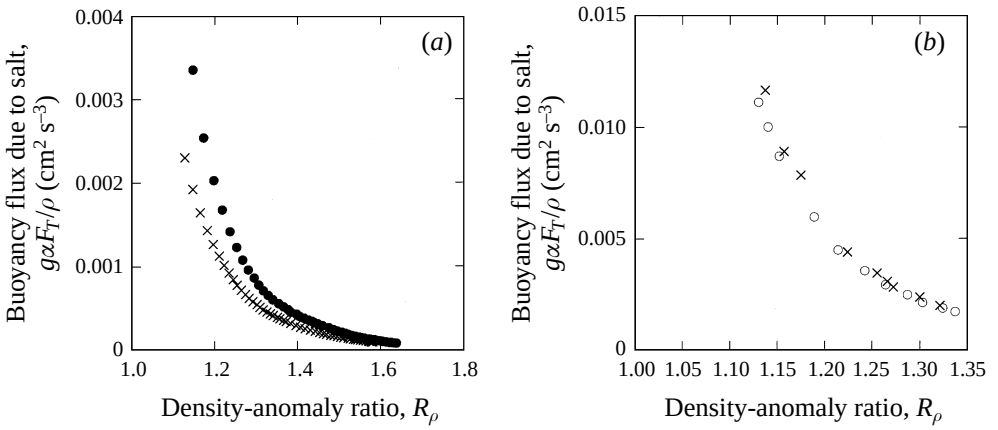

FIGURE 19. $g\alpha F_T/\rho$ *vs.* R_ρ for experiments started with the same solute concentrations but having different coupling modes. (*a*) UA1*a*(×) and UA1*c*(•). The latter flow was characterized by a flow pattern consisting of two interfacial waves, and this gives rise to increased fluxes. (*b*) ANU1.3*a* (◯) and Stamp & Griffiths's (1997) annulus experiment 2*a* (×). The fluxes were similar for the two cases in (*b*) despite the fact that the annulus flow consisted of waves and convection cells that travelled in a circular path.

coupling modes. For example, experiments UA1*a, c* were both started with the same solute concentrations and in the same channel but the latter exhibited a flow pattern consisting of two interfacial waves each travelling in a circular path around half the channel. The salt flux for these experiments is shown in figure 19(*a*), and it is clear that the different mode gives rise to increased fluxes, especially at low R_ρ where the coupling is strong. In contrast, the fluxes for experiment ANU1.2 are close to those measured by Stamp & Griffiths (1997) for a similar experiment carried out in an annulus (figure 19*b*). This latter flow consisted of waves and convection cells that both travelled in a circular path, and hence the similar fluxes might result from this flow being a periodic extension of that in the rectangular channel.

To summarize, with it not being possible to set up flows without coupling, determining the effect of coupling on the fluxes necessitated comparing the measured fluxes with those from a model of a uniform interface. A numerical extension to Linden & Shirtcliffe's (1978) approximate analytical model was therefore developed. As expected, subsequent comparison indicates that at low R_ρ, where there are significant variations in interface thickness and strong large-scale circulations, the fluxes are increased, whereas at high R_ρ where the coupling is weak the fluxes are unaffected. In addition, experiments with different modes of coupling indicate that fluxes depend on the exact nature of the flow. These issues warrant further attention however, with more accurate measurements and using flows dominated by viscous dissipation at the tank sidewalls as a basis for comparison.

7. Variations on a theme

The flows described above have all been characterized by a single aqueous salt–sugar interface separating two layers of depth 11.5–12.0 cm. In this section other geometries and solutions are examined, and the possibility of wave–convection coupling in oceanic staircases then discussed.

7.1. *Variations in tank and cell geometries*

For two-layer flows in rectangular channels the important geometrical parameters are the depth ratio H_u/H_l and the channel aspect ratios L/w and L/H_u. Additional salt–sugar experiments were carried out to determine the geometries for which wave–convection coupling occurs.

The scaling arguments indicate that once the convection becomes organized into large-scale circulations the convective velocities depend on the channel length via (9), rather than the layer depth (Hunt 1984). This result implies that coupling can occur when the layer depths are different. To test this assertion an experiment was carried out in the 15×5 cm channel with $H_u = 5.75$ cm and $H_l = 11.5$ cm layers, i.e. the Rayleigh number for the upper layer was an order of magnitude less than that for the lower layer. As expected, the long-term flow was indistinguishable from flows with two layers of equal depth; a single wave propagated back-and-forth along the channel, the flow in the upper layer was a mirror image of that in the lower layer, and the wave speeds were similar to those for the $H = 11.5$ cm flows.

In previous experiments the minimum channel width was 5 cm and the wave speed decreased in response to changes in the layer properties rather than viscous dissipation at the sidewalls. To investigate the behaviour of flows for which sidewall dissipation is important, experiments were carried out in a channel of cross-section 15×2.5 cm. At first the flow evolved in the usual manner, with several interfacial waves forming and organizing the convection into circulations on the scale of the distance between waves. However, the sidewall dissipation slowed the convective motions, and they soon became too weak to maintain the thick regions of interface.

To determine the effects of variations in absolute layer depths, experiments were also carried out in the 15×5 cm channel with two layers of depth $H = 2.5$ cm. The small volume of each layer resulted in more rapid changes in layer properties, and, as a result, interfacial waves formed immediately after filling. Further evolution was not observed, with the thick and thin regions of the interface disappearing before a single wave formed. This behaviour probably occurred because the system evolved through the critical R_ρ regime for coupling before the flow could become organized. However, it is also possible that the nature of the waves changed in response to the change in the relative magnitudes of the total depth of fluid, the thickness of the thin interface, the thickness of the thick interface and the length of the thick region.

7.2. *Variations in the double-diffusive system*

Other experiments demonstrated that wave–convection coupling occurs for a wide range of solutions including glycerol above aqueous potassium carbonate solution and cold fresh water above hot salt water. In the former case, however, coupling only occurred for dilute glycerol solutions where the viscosity contrast across the interface was small. As expected, coupling did not occur for interfaces formed by heating a stable two-layer salt-stratified fluid from below. In this configuration the convective motions of the lower layer were dominated by the buoyancy flux through the bottom boundary rather than that through the diffusive interface.

7.3. *Multiple diffusive interfaces*

The behaviour of a three-layer system was also investigated. A salt layer above two sugar layers was set up in the 15×15 cm channel with layers of depths $H_u = H_l = 10$ cm and $H_m = 5$ cm. Initially a diffusive interface formed between the upper (salt) and middle (sugar) layers, while the interface between the middle (sugar) and lower (sugar) layers remained inactive. However, once the salt concentration

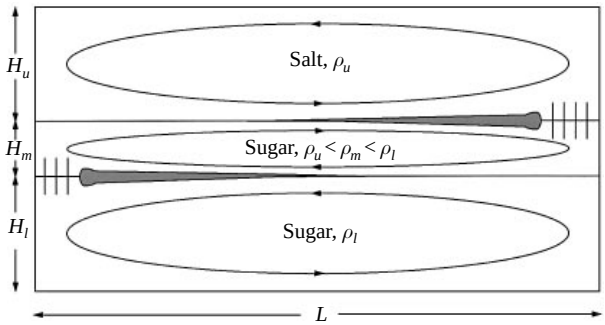

FIGURE 20. Illustration of the flow with multiple interfaces. A three-layer system was set up with a salt layer above two sugar layers. The diffusive interface between the upper and middle layers transported salt into the middle layer, and, as a result, a diffusive interface formed between the middle and lower layers. After about an hour a single wave propagated back-and-forth along each interface. The waves were exactly out of phase, and the convection in each layer was organized into large-scale cells which reversed direction quasi-periodically, with the middle layer rotating in the opposite direction to its neighbours.

in the middle layer increased, a diffusive interface formed between the middle and lower layers. After about an hour each interface supported a single wave. The waves propagated back-and-forth along the channel exactly out of phase, so that the top wave propagated to the right while the bottom wave propagated to the left (figure 20). In turn, the convection in each layer was organized into large-scale cells which reversed direction quasi-periodically, with the middle layer rotating in the opposite direction to its neighbours. This flow continued until the middle layer became denser than the lower layer and overturning occurred.

7.4. *Implications for oceanic interfaces*

With wave–convection coupling occurring for a wide range of cell geometries, and Stamp & Griffiths (1997) finding that in annular and square cavities coupling produces turbulent convection cells of a travelling-wave nature coupled to waves on the interface, it is of interest to consider whether coupling can occur in the ocean.

Diffusive staircases have been observed throughout the world's oceans and make an important contribution to vertical mixing (Schmitt 1994). At high latitudes the cold winds and high precipitation produce cold fresh water that overlies hot salty water produced at low latitudes, and the unusually weak internal wave field allows low-flux, high-R_ρ, interfaces to remain stable; for example Padman & Dillon (1987) found $1 \leqslant R_\rho \leqslant 10$ in the Canada Basin. However, the mid-latitudes are generally less favourable to diffusive staircases, with observations showing such staircases to be characterized by high-flux, $1 \leqslant R_\rho \leqslant 3$, interfaces because the strong internal wave field disrupts low-flux interfaces (Kelley 1984).

As described in § 5, the salt–sugar system only supported coupling for critical c/u values,

$$0.39 \leqslant c/u \leqslant 0.54. \tag{23}$$

We proceed on the assumption that a similar matching is required between the wave speed and the convective velocities for coupling to occur in the heat–salt systems in the ocean.

Substituting (10) and (9) for the wave speed and convective velocity, respectively,

and then using the diffusive scale,

$$h_T = \rho\kappa_T(\alpha\Delta T)/\alpha F_T, \tag{24}$$

to estimate $h(\alpha\Delta T, R_\rho)$, allows the inequality to be expressed in terms of the non-dimensional parameters:

$$\frac{0.39}{f(a/h)_{c/u=0.39}} \leqslant \left(\frac{g^2\kappa_T}{B_*}\right)^{1/2} [(B_*L)^{-1/3}(\alpha\Delta T)^{-1/9}(R_\rho - 1)^{1/2}F_T^{*-5/6}(1-\tau^{1/2})^{-1/3}]$$
$$\leqslant \frac{0.54}{f(a/h)_{c/u=0.54}}. \tag{25}$$

The measured parameters of the salt–sugar system given in table 1 for the onset and suppression of coupling (at $c/u = 0.39$ and 0.54, respectively) were used to determine the unknown values of the amplitude function in (25). These were

$$f\left(\frac{a}{h}\right)_{c/u=0.39} = 0.39 \pm 0.04 \tag{26a}$$

and

$$f\left(\frac{a}{h}\right)_{c/u=0.54} = 0.19 \pm 0.02, \tag{26b}$$

which to a good approximation were constant over the range of experiments. It should be noted that, although $f(a/h)$ depends explicitly on τ and L (see (12 *a*)), this dependence has been allowed for by the $(1-\tau^{1/2})^{-1/3}$ and $L^{-1/3}$ terms in the inequality. Thus the constants in (26 *a,b*) are expected to be independent of τ and L, allowing the inequality (25) to be applied to any double-diffusive system for which $F_T^*(R_\rho, \tau)$ is known. However, in order to apply the inequality to a heat–salt system in the ocean, it is not clear what value of L is appropriate and, for the moment, this is left as a parameter. To enable comparison with oceanic measurements, (25) may be written as

$$1 \leqslant \left(\frac{g^4\kappa_T}{B_*^3}\right)^{5/18} G^{-4/9}\left(\frac{D}{L}\right)^{1/3}(R_\rho - 1)^{1/2}F_T^{*-5/6}(1-\tau^{1/2})^{-1/3} \leqslant 2.9, \tag{27}$$

where

$$G = \left(\frac{D^3 g\alpha\Delta T}{\kappa_T^2}\right)^{1/4} \tag{28}$$

is the non-dimensional scale for layers of thickness D in a staircase. Here G is equivalent to that used by Kelley (1984, 1988) with the average buoyancy frequency $\overline{N} = (g\alpha\Delta T/D)^{1/2}$. A regime diagram plotted in figure 21 summarizes the coupling criteria (27) for several values of the aspect ratio D/L which might characterize a convection cell. Also shown are the oceanic measurements from Kelley (1984) and Padman & Dillon (1987) which coincide, particularly for $R_\rho < 5$, with regimes where coupling is predicted to occur for a number of different cell aspect ratios D/L. In the ocean, where channel sidewalls do not fix the cell aspect ratio, we anticipate that a different mechanism will constrain the cell geometry. However, an investigation of this is beyond the scope of the current study.

The preceding analyses suggest that coupling is possible for oceanic T and S profiles, and thus the effect of other oceanic processes, notably internal waves, on coupling should be determined. Two main possibilities exist. First, internal waves might produce large enough variations in the thickness of a diffusive interface to alter

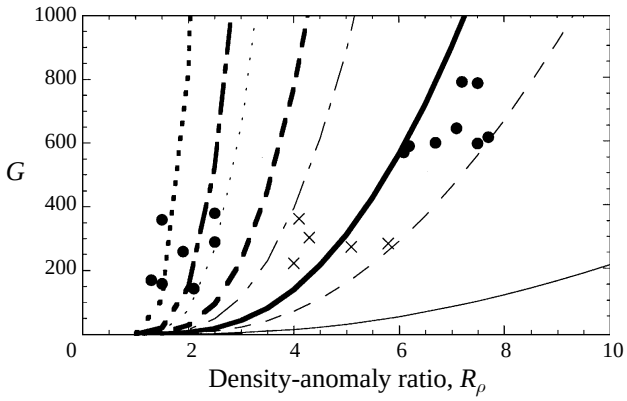

FIGURE 21. Comparison of oceanic measurements with the regimes where coupling is predicted to occur, as a function of the parameters G and R_ρ. Curves are plotted for a number of different aspect ratios which might characterize convection cells, with coupling predicted between the onset curve (shown in bold weighting) and the suppression curve (shown in normal weighting): $D/L = 0.001$ (———), $D/L = 0.01$ (- - - - -), $D/L = 0.1$ (– - – -) and $D/L = 1$ (·····). The measurements from Kelley (1984) are shown as (•) and those made by Padman & Dillon (1987) by (×).

the interfacial fluxes, and thereby disrupt, or trigger, coupling. This scenario is unlikely however, because the waves that produce large strains have frequencies near twice the Coriolis frequency, or periods of about six hours for the Canada Basin, (Pinkel *et al.* 1991) whereas coupling occurs on a much smaller time scale. Second, ambient shear, which is largely produced by internal waves, could decouple the interfacial wave from the buoyancy anomalies in the surrounding layers. Again a separation of time scales renders this scenario unlikely, with Anderson (1992) showing that the waves that produce the most shear have frequencies near the Coriolis frequency, i.e. periods of 12 hours for the Canada Basin.

To summarize, extrapolation from salt–sugar experiments predicts that long-term coupling is likely to occur in heat–salt systems at low values of R_ρ, the exact range being mainly dependent upon the convective cell geometry. Physical reasoning suggests that the time scale associated with the oceanic internal wave field is sufficiently long so as to allow long-term coupling to exist in mid- and high-latitude oceanic staircases. The implication of this behaviour for mixing is that the fluxes through a staircase are likely to be significantly enhanced over those expected by neglecting coupling. Moreover, although coupling is not expected for R_ρ values below the onset threshold, the interfacial fluxes should still be increased due to the presence of thick and thin regions of interface. Such issues require more detailed investigation.

8. Summary and conclusions

A series of experiments showed that when layers of salt and sugar solution were superimposed with a diffusive interface between, interfacial waves were spontaneously generated by the turbulent convection once the system evolved to a critical value of the density-anomaly ratio. The waves locally modulated the interfacial buoyancy flux by modifying the interface thickness and thereby organized the otherwise random convective motions into large-scale circulations. Subsequent interactions between the

waves and convection led to a decrease in the number of waves and an increase in the scale of the convective circulations.

In rectangular channels a single wave propagated back-and-forth along the channel for a wide range of conditions. The waves consisted of a short thick solitary-wave nose followed by a long thin tail which was acted upon by gravity and the stress exerted by the convection. As the wave traversed the channel, intense plumes at the nose organized the convection in each layer into two large-scale cells which slowed the nose while sweeping the tail forward. The cells ahead of the wave disappeared when the wave collided with an endwall, and the tank-scale circulations then swept the interfacial fluid against the endwall increasing the thickness of the wave before it collapsed outwards.

The waves persisted for about 4 hours and travelled 20 m, whereas solitary waves propagating along a slightly diffused density interface between two deep motionless layers of constant density only exist for about 2 minutes and travel 3 m (Stamp & Jacka 1995). Hence the wave gained enough energy from the convection to overcome the dissipative effects of viscous stresses, turbulent mixing and wave radiation. Indeed, it is reasonable to expect that the waves would have propagated indefinitely had the convection not run down. The coupling was found to be most effective when the interface was thick enough to support waves of sufficient amplitude and speed to match the convective velocities, but not so thick as to greatly reduce the interfacial fluxes and convective velocities. A plausible explanation of this result is that it ensures that the wave's tail, which was swept along by the convection, remains attached to the propagating nose, and this is required if the horizontal variations in the thickness of the interface are to remain coherent.

The recognition that waves and convection can couple together and reinforce each other to produce dramatic phenomena is relevant because similar interactions might also occur in other laboratory and geophysical flows. Stamp & Griffiths (1997) report striking similarities between the flow in an annulus and that of an atmospheric squall line. In addition, the flow in a rectangular channel bears some resemblance to the El Niño–Southern Oscillation phenomenon (Bjerknes 1969), in that for both systems there is an oscillatory change in large-scale convective circulations when waves reflect back-and-forth along a channel. There is, however, an important difference between these two systems. In the El Niño–Southern Oscillation large heat and water vapour fluxes in the western Pacific strengthen westward winds, which in turn lead to larger sea surface temperature gradients and larger fluxes. This 'positive feedback' tends to maintain the normal state of the system and thus perturbations are required to reverse the circulations. In contrast, the double-diffusive system exhibited 'negative feedback' because when the wave was at one end of the channel the buoyancy flux opposed the existing circulations, and eventually the circulations were forced to reverse.

Turning to the relationship between this work and previous studies of double-diffusive convection, we interpret the described flow as the turbulent counterpart to the 'travelling-wave' pattern of convection cells observed at marginally unstable conditions in fluids subject to linear heat and salt gradients (Knobloch *et al.* 1986). Moreover, the present experiments demonstrate that the manner in which a diffusive interface is formed is important; whereas the flow surrounding an interface formed by heating a stable two-layer salt stratification from below is random, that surrounding an interface formed when a cold fresh layer is floated above a denser hot salt layer is organized so as to minimize the shear across the interface. This difference should be taken into account when comparing experiments with observations, and casts doubt, for example, on the general application of Kelley's (1988) postulate that the thickness

of layers in a diffusive staircase is set by the susceptibility of the interfaces dividing each layer to (random) convection-driven shear instabilities.

Most previous studies of double-diffusive convection have focused on determining empirical flux laws for extrapolation to geophysical and technological settings. Here comparison of the measured fluxes with those from a numerical model of a uniform interface suggests that the wave–convection coupling led to a doubling of fluxes at low R_ρ. Such an increase is plausible because the gradients across the thin interface ahead of the wave were much larger than would be the case if the interface were rearranged to be of uniform thickness, and the large-scale circulations maintained these thin regions by sweeping the interfacial fluid to the wave. In addition, experiments started with the same solute concentrations but having different coupling modes produced different fluxes, thus indicating that there are no 'correct' fluxes for given $(\alpha\Delta T, R_\rho)$. Both these results suggest that the coupling process should be included in theoretical models used to predict fluxes, and that caution is needed when extrapolating experimental flux measurements to other settings.

Finally, before the described laboratory flow is fully understood, the exact nature of energy transfer from the convection to the wave must be determined. Clarification of the coupling mechanisms should also ascertain whether the short-time-scale wave speed variations resulted from random noise or deterministic chaos, and test the suggestion that the changes in coupling during run-down were due to changes in the structure of the interface. The best approach to such questions is unclear, however, because mathematical models are difficult to formulate and numerical models require high resolution. Nevertheless, this and other strongly nonlinear phenomena involving the interaction of large-amplitude waves and turbulent convection are worthy of further investigation as their role in Nature is not yet clear.

This work was done while A.P.S. was a PhD student in the Geophysical Fluid Dynamics Group, Research School of Earth Sciences, The Australian National University. A.P.S. & R.W.G. appreciate the helpful comments of Professor J. S. Turner, and the technical assistance provided by Derek Corrigan and Ross Wylde-Browne. G.O.H. is grateful for the financial support of IPENZ and McConnell Dowell Corporation Ltd. The manuscript was prepared while A.P.S. was at the School of Oceanography, University of Washington (supported by the UCAR Visiting Scientist Program), and G.O.H. was at the Department of Applied Mathematics and Theoretical Physics, University of Cambridge (supported by the Association of Commonwealth Universities), and later, at EnFlo, Department of Mechanical Engineering, University of Surrey (supported by NERC). We also appreciate the assistance of Dr T. G. L. Shirtcliffe, who graciously sifted through his original data and then supplied corrected values of his non-dimensional fluxes, and Dr Kelley who provided the data plotted in figure 17(*b*).

Appendix. Extensions to Linden & Shirtcliffe's (1978) model

Linden & Shirtcliffe (1978) proposed a mechanistic model of the double-diffusive transport across a diffusive interface. The interface was modelled as having a stably stratified core sandwiched between two unstable boundary layers, and to obtain analytical results it was further assumed that the gradients through the core are linear and remain constant, and that the core is much thicker than the boundary layers. A one-dimensional numerical model of the diffusive interface was developed to test these assumptions.

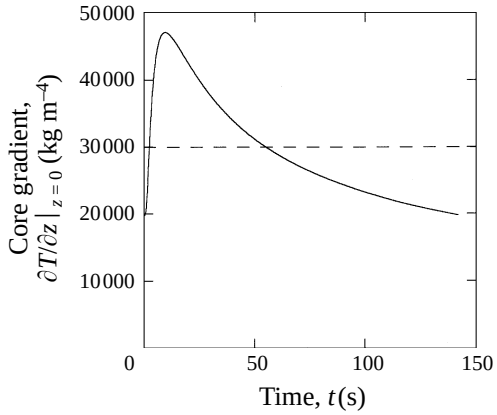

FIGURE 22. Salt gradient at the centre of the core, $\partial T/\partial z|_{z=0}$ (———), during the course of a steady-state cycle for $R_\rho = 1.2$ and $\alpha\Delta T = 0.03$, and the corresponding value used by Linden & Shirtcliffe (1978) (— — —).

The numerical model solved the one-dimensional diffusion equations used by Linden & Shirtcliffe (1978) for the T and S profiles using a simple time-stepping finite difference scheme initialized with two well-mixed layers separated by step discontinuities of ΔT and ΔS (figure 1a). At each time step the diffusion equation was resolved until the boundary layers had grown thick enough to meet the Rayleigh number criterion for instability used by Linden & Shirtcliffe (1978), and the entire boundary layer was then removed. The remaining T and S stratifications were then used as initial conditions for the next cycle of boundary layer growth, and after several such cycles the model converged to a steady cyclic behaviour.

Numerical solutions obtained in this manner indicate that at low R_ρ, both of Linden & Shirtcliffe's (1978) assumptions are violated, and figure 22 shows the variation in the T gradient through the core during a steady-state cycle. This variation occurs because at the start of the cycle the discontinuity in the T stratification produces large gradients and fluxes. However, as unstable fluid accumulates in the boundary layers the gradients across the core decrease and in turn the diffusive fluxes decrease. In addition, with the thickness of the core being small when the core gradients are large, this behaviour also implies that the core varies in thickness during a cycle.

To compare the fluxes from the numerical model with the measured values and those of Linden & Shirtcliffe (1978), the instantaneous fluxes were averaged over a cycle. As shown in figure 17(a), the analytical values are surprisingly close to the numerical predictions, with this agreement occurring because the core gradients used by Linden & Shirtcliffe (1978) are close to the cycle-averaged values of the numerical model.

REFERENCES

ANDERSON, S. P. 1992 Shear, strain and thermohaline vertical fine structure in the upper ocean. PhD thesis, University of California, San Diego.

BJERKNES, J. 1969 Atmospheric teleconnections from the equatorial pacific. *Mon. Weather Rev.* **97**, 163–172.

CRAPPER, P. F. 1975 Measurements across a diffusive interface. *Deep-Sea Res.* **22**, 537–545.

GRIFFITHS, R. W. & RUDDICK, B. R. 1980 Accurate fluxes across a salt-sugar finger interface deduced from direct density measurements. *J. Fluid Mech.* **99**, 85–95.

HUNT, J. C. R. 1984 Turbulence structure in thermal convection and shear-free boundary layers. *J. Fluid Mech.* **138**, 161–184.

HUPPERT, H. E. & TURNER, J. S. 1981 Double-diffusive convection. *J. Fluid Mech.* **106**, 209–329.

KELLEY, D. E. 1984 Effective diffusivities within oceanic thermohaline staircases. *J. Geophys. Res.* **89**, 10484–10488.

KELLEY, D. E. 1988 Explaining effective diffusivities within diffusive oceanic staircases. In *Small-Scale Turbulence and Mixing in the Ocean* (ed. J. C. J. Nihoul & B. M. Jamart), pp. 481–502. Elsevier.

KELLEY, D. E. 1990 Fluxes through diffusive staircases: A new formulation. *J. Geophys. Res.* **95**, 3365–3371.

KNOBLOCH, E., DEANE, A. E., TOOMRE, J. & MOORE, D. R. 1986 Doubly diffusive waves. *Contemp. Maths* **56**, 203–216.

LINDEN, P. F. 1974 A note on the transport across a diffusive interface. *Deep-Sea Res.* **21**, 283–287.

LINDEN, P. F. & SHIRTCLIFFE, T. G. L. 1978 The diffusive interface in double-diffusive convection. *J. Fluid Mech.* **87**, 417–432.

MARMORINO, G. O. & CALDWELL, D. R. 1976 Heat and salt transport through a diffusive thermohaline interface. *Deep-Sea Res.* A **23**, 59–67.

MCDOUGALL, T. J. 1981 *a* Double-diffusive convection with a non-linear equation of state: Part 1. the accurate conservation of properties in a two-layer system. *Prog. Oceanogr.* **10**, 71–89.

MCDOUGALL, T. J. 1981 *b* Double-diffusive convection with a non-linear equation of state: Part 2. laboratory experiments and their interpretation. *Prog. Oceanogr.* **10**, 91–121.

NEWELL, T. A. 1984 Characteristics of a double-diffusive interface at high density stability ratios. *J. Fluid Mech.* **149**, 385–401.

PADMAN, L. & DILLON, T. M. 1987 Vertical heat fluxes through the Beaufort Sea thermohaline staircase. *J. Geophys. Res.* **92**, 10799–10806.

PINKEL, R., SHERMAN, J., SMITH, J. & ANDERSON, S. 1991 Strain: Observations of the vertical gradient of isopycnal vertical displacement. *J. Phys. Oceanogr.* **21**, 527–540.

RUDDICK, B. R. & SHIRTCLIFFE, T. G. L. 1979 Data for double diffusers: Physical properties of aqueous salt-sugar solutions. *Deep-Sea Res.* **26**, 775–787.

SCHMITT, R. W. 1994 Double diffusion in oceanography. *Ann. Rev. Fluid Mech.* **26**, 255–285.

SHIRTCLIFFE, T. G. L. 1973 Transport and profile measurements of the diffusive interface in double diffusive convection with similar diffusivities. *J. Fluid Mech.* **57**, 27–43.

SIGGIA, E. D. 1994 High Rayleigh number thermal convection. *Ann. Rev. Fluid Mech.* **26**, 137–168.

STAMP, A. P. & GRIFFITHS, R. W. 1997 Turbulent travelling-wave convection in a two-layer system. *Phys. Fluids* **9**, 963–969.

STAMP, A. P. & JACKA, M. 1995 Deep-water internal solitary waves. *J. Fluid Mech.* **305**, 347–371.

TAYLOR, J. 1988 The fluxes across a diffusive interface at low values of the density ratio. *Deep-Sea Res.* **35**, 555–567.

TURNER, J. S. 1965 The coupled turbulent transports of salt and heat across a sharp density interface. *Intl J. Heat Mass Transfer* **8**, 759–767.

TURNER, J. S. 1974 Double-diffusive convection. *Ann. Rev. Fluid Mech.* **6**, 37–56.

TURNER, J. S. 1985 Multicomponent convection. *Ann. Rev. Fluid Mech.* **17**, 11–44.

TURNER, J. S. & CHEN, C. F. 1974 Two-dimensional effects in double-diffusive convection. *J. Fluid Mech.* **63**, 577–592.